RESEARCH ARTICLE | MARCH 04 2024

Energetic and dynamic characterization of pollutant dispersion in varied building layouts through an augmented analysis procedure

Special Collection: Flow and Civil Structures

Yunfei Fu (云飞 付) ; Cruz Y. Li (雨桐 李) ; Zhihang Zhao (智航 赵) ; Bingchao Zhang (秉超 张) ; K. T. Tse (锦添 谢) ; Cheuk Ming Mak (卓明 麥) ; Zengshun Chen (增顺 陈) ; Xinxin Feng (欣鑫 冯) ; Xisheng Lin (习升 蔺) ; Wenxin Li (雯欣 李) ✉ ; Chongjia Lin (崇佳 林) ✉

Physics of Fluids 36, 035105 (2024)
https://doi.org/10.1063/5.0190268

Physics of Fluids ARTICLE pubs.aip.org/aip/pof

Energetic and dynamic characterization of pollutant dispersion in varied building layouts through an augmented analysis procedure

Cite as: Phys. Fluids **36**, 035105 (2024); doi: 10.1063/5.0190268
Submitted: 5 December 2023 · Accepted: 30 January 2024 ·
Published Online: 4 March 2024

Yunfei Fu (云飞 付),[1,a)] Cruz Y. Li (雨桐 李),[2,b)] Zhihang Zhao (智航 赵),[2,c)] Bingchao Zhang (秉超 张),[3,d)] K. T. Tse (锦添 谢),[3,e)] Cheuk Ming Mak (卓明 麥),[1,f)] Zengshun Chen (增顺 陈),[2,g)] Xinxin Feng (欣鑫 冯),[3,h)] Xisheng Lin (习升 藺),[3,i)] Wenxin Li (雯欣 李),[1,j)] and Chongjia Lin (崇佳 林)[4,j)]

AFFILIATIONS

[1]Department of Building Environment and Energy Engineering, The Hong Kong Polytechnic University, Hung Hom, Kowloon, Hong Kong, China
[2]School of Civil Engineering, Chongqing University, Chongqing 400045, China
[3]Department of Civil and Environmental Engineering, The Hong Kong University of Science and Technology, Clear Water Bay, Kowloon, Hong Kong, China
[4]Department of Mechanical and Aerospace Engineering, The Hong Kong University of Science and Technology, Clear Water Bay, Kowloon, Hong Kong, China

Note: This paper is part of the special topic, Flow and Civil Structures.
[a)]**Electronic mail:** yfuar@connect.ust.hk
[b)]**Electronic mail:** cruzli@cqu.edu.cn
[c)]**Electronic mail:** zhaozhihang@cqu.edu.cn
[d)]**Electronic mail:** timkttse@ust.hk
[e)]**Electronic mail:** zhangbc@ust.hk
[f)]**Electronic mail:** cheuk-ming.mak@polyu.edu.hk
[g)]**Electronic mail:** zengshunchen@cqu.edu.cn
[h)]**Electronic mail:** u3007314@connect.hku.hk
[i)]**Electronic mail:** xlinbl@connect.ust.hk
[j)]**Authors to whom correspondence should be addressed:** wenxinn.li@connect.polyu.edu.hk and clinag@connect.ust.hk

ABSTRACT

This work presents a post-data analysis procedure, namely, proper orthogonal decomposition (POD)–dynamic mode decomposition (DMD)–discrete Fourier transform analysis, for evaluating the dominant features of the flow fields from both energetic and dynamic perspectives. The large-eddy simulation (LES) was first employed to reproduce the flow field surrounding three types of building layouts. Subsequently, both POD and DMD were conducted according to LES simulation results. The extracted modes were classified into three types based on the POD and DMD: Type-1 mode: energetically and dynamically significant mode, Type-2 mode: energetically significant and dynamically insignificant mode, and Type-3 mode: energetically insignificant and dynamically significant mode. The findings indicate that Type-1 mode governs the primary velocity field and the predominant vortex patterns observed at the rear of the building arrays, as the reduction of inter-building widths leads to a shorter flow separation region. Type-2 mode is characterized by the presence of small-scale vortices and the high turbulent kinetic energy region, which periodically triggers pollutant increase in the vicinity of structures. Type-3 mode demonstrates a minimal energetic influence on the flow field; nevertheless, it significantly contributes to the consistent build-up of pollutants within the far-wake region. The present study also investigates the predominant coherent structures of flow fields concerning various building layouts and highlights the influence of passage widths on the efficiency of pollutant removal. This comprehensive analysis enables a systematic exploration of flow patterns within various building layouts, offering potential solutions for pollutant dispersion challenges in metropolitan areas.

NOMENCLATURE

Latin letters

A	Infinite-dimensional Koopman operator
$\tilde{A}$	Similarity-matrix approximate of A
a_j	Temporal coefficient of POD mode
C_S	Smagorinsky constant
C_μ	Model constant
g_j	DMD Mode growth/decay rate
H	Reference height
k	Turbulent kinetic energy
$LESIQ_\upsilon$	Index for LES grid resolution
$\bar{p}$	Filtered pressure
S	Covariance matrix
$\overline{S_{ij}}$	Strain rate tensor
U	Matrix containing all POD mode
u'	Fluctuation velocity
u^*	ABL friction velocity
U_{ref}	Reference velocity
$\overline{u_i}$	Filtered velocity
u_p	Instantaneous velocity components tangential to the wall
V	Matrix containing temporal information of U
V_{cell}	Cell volume
w_j	DMD mode frequency
X^n	Snapshot sequence from 1 to n − 1
X^{n+1}	Snapshot sequence from 2 to n
y^+	Average non-dimensional wall distance
y_i	Eigenvalues of DMD mode
z_0	Roughness length
Δt	Time steps
Δz	Vertical size of the cell volume next to the wall
μ	Air dynamic viscosity
μ_p	Instantaneous velocity components tangential to the wall
ρ	Density
τ_{ij}	Subgrid-scale model stress tensor
τ_w	Instantaneous wall-shear stress.
φ_i	Eigenvectors of DMD mode
υ_T	Eddy viscosity

Greek symbols

Δ	3D filter size
Δt	LES simulation time steps
κ	The Von Karman constant
λ_j	Eigenvalues of jth POD mode
υ	Kinematic viscosity
Φ	DMD mode matrix
ϕ_j	jth POD mode matrix
ψ_j	jth Eigenvectors of covariance matrix S
Σ	Diagonal matrix containing all singular values of matrix U

Others

$\|\|$	$\|\|_F$ Frobenius normalization

I. INTRODUCTION

The rapid development of urban areas worldwide has led to a significant increase in the demand for fossil fuel energy to support transportation, indoor temperature regulation, and industrial production.[1,2] However, this growth has also led to the emergence of densely populated urban regions, characterized by numerous skyscrapers clustered within a small area, which has raised concerns regarding air ventilation restrictions.[3] The research on sustainable cities will increasingly become indispensable in the forthcoming years as a means of reducing air pollution, mitigating the impacts of urban heat islands (UHI), and managing global warming.[4–6] Moreover, the constricted roadways in urban areas frequently experience high vehicular traffic during peak hours, resulting in increasing risks of respiratory diseases, such as tracheitis and lung cancer, among city dwellers.[7,8] The flow characteristics and pollutant dispersion in street canyons are closely interconnected and many previous studies have investigated the flow and dispersion characteristics in urban areas.[9] The flow patterns within street canyons, characterized by intricate turbulence, are widely recognized as governing pollutant dispersion, and exhibit a strong correlation with flow patterns in two-dimensional canyons.[10] The distribution of pollutant concentrations in street canyons can predominantly described by the structure of the turbulence and vortex circulation.[11] Therefore, to enhance the comprehension of pollutant dispersion in street canyons, it is imperative to investigate the flow characteristics and the flow-diffusion mechanisms in urban wind environments, particularly at pedestrian-level height. Therefore, conducting a comprehensive analysis of the flow-diffusion mechanisms in urban wind environments, particularly at the pedestrian level is imperative. By elucidating the intricate flow patterns of turbulence at the pedestrian level in urban areas, researchers and policymakers can devise strategies to mitigate the adverse effects of urbanization on air quality and public health.

In recent decades, computational fluid dynamics (CFD) has been widely used in predicting wind fields in urban street canyons due to the rapid development of computational resources.[12,13] Despite its widespread application in urban environments, the steady Reynold-averaged Navier–Stokes (RANS) model fails to capture the transient features of urban wind and often leads to an overestimation of the wake region surrounding buildings.[14,15] Recent years have witnessed a growing emphasis on the application of large eddy simulation (LES) for studying pollution dispersion.[16,17] LES can reproduce large-scale unsteady motions, and it has been demonstrated that it can accurately delineate the dynamic flow characteristics within the building array.[18–22] Given the highly turbulent and complex nature of the flow field within building arrays, this study employs large eddy simulation (LES) to further investigate the pollution dispersion mechanism at the pedestrian level.

Considerable research has been conducted on the flow characteristics and complexities of pollutant diffusion in urban areas,[23] taking into consideration influential factors such as canyon geometry,[24] inner barriers (vegetation, balconies and vehicles),[25–29] as well as other meteorological parameters including temperature and air pressure.[30] Li *et al.* highlighted the complexity of pollutant transportation in the urban environment and further mentioned that the situation becomes more intricate with varying distances of wind corridors.[17] Hang and Li examined the ventilation flow rates and air change rates in building clusters, and their findings suggested that variations in building height contribute to an enhancement of vertical flow.[31] Shen *et al.* employed LES to investigate pollutant dispersion within urban canopies and revealed a significant variation in pollution concentration with respect to building density.[11] Hassan *et al.* used LES to simulate the pollutant dispersion within street canyons and discovered that neighboring vortices interact resulting in a deceleration of pollutant removal in the vicinity of buildings.[32] Miao *et al.* investigated the influence of urban street canyon morphology on suspended particulate matter concentration at the pedestrian level and demonstrated a significantly lower concentration of pollutants in high-rise building areas compared to multilayer building areas.[33]

Published literature has addressed the relationship between building layouts and pollutant diffusion; however, the computational costs associated with LES are substantial. Instead of conducting repetitive LES case studies, it is of paramount to identify the spatially and temporally dominant flow field structures responsible for pollutant dispersion within street canyons. Therefore, the application of appropriate post-processing techniques that are capable of extracting the spatial and temporal characteristics of flow field structures is crucial. In recent years, a multitude of reduced-order models (ROMs) have emerged as invaluable instruments for extracting spatial features and dynamical properties from numerical simulation and experimental data in analyzing pollutant dispersion in urban area.[34–36] To elucidate the flow structure within complex turbulence, researchers have introduced a variety of flow field decomposition algorithms, proper orthogonal decomposition (POD) is one of the typical eigenvector decomposition methods introduced by Lumley. This method facilitates the decomposition of a dataset into basis modes, aiding in the identification of the most energetic content.[37] POD has been demonstrated to be a proficient method for identifying dominant coherent structures based on their energy contributions, and it has gained extensive application in air pollution analysis due to its efficiency and precision.[38–40] Bieringer *et al.* proposed a method enabling the characterization of POD for a given sampling period, which has been successfully applied in urban environments.[38] Fang *et al.* incorporated POD into an air pollution model in urban street canyon and highlighted that POD solutions exhibit a high level of consistency with the results from the full finite-element model, while significantly reducing computational requirements.[39] However, this approach is inapplicable to fluid–structure interaction for the fluid velocity field, because the fluid domain is time-variant and the POD modes exhibit orthogonality properties in spatial domains, thus are not time-dependent, deducing the temporal evolution of the dynamic system is beyond the ability of POD.[41,42] Furthermore, multiple dominant frequencies can be identified in each mode, determining the flow pattern of the dominant frequency within each POD mode remains challenging and it is difficult to discern low-energy modes that significantly contribute to the flow field data via POD.[43]

Another data-driven flow field decomposition method is dynamic mode decomposition (DMD) introduced by Schmid,[44] which is capable of identifying potential spatial-temporal dynamics characteristics by extracting key parameters.[42] In contrast to POD, DMD can capture a unique frequency for each decomposition mode and describe specific dynamic features from spatial and temporal perspectives. The efficacy of DMD in elucidating flow structures and dynamic features in various disciplines has been demonstrated by numerous studies.[45] The application of DMD in the wind engineering field has been an area of intense investigation in recent years. Zhang *et al.* employed DMD to investigate the wake of the bridge model to identify the dominant wake flow structures and concluded that the vortex generator significantly alters the energy spectrum. This is the first attempt to utilize the DMD in flow field analysis.[46] Li *et al.* applied DMD to pressure flow field analysis and concluded that DMD can provide accurate and practically advantageous results in wind engineering applications.[45] Guissart *et al.* employed DMD on the numerical and experimental spatiotemporal pressure coefficient to understand the unsteady features of flow around a rectangular cylinder and corroborated the influence of incidence angles on coherent structures.[47] Additionally, some mode selection criteria are usually coupled with DMD such as α-criteria[48] and I-criteria[49] to rank the modes based on dynamical influences. However, DMD is deficient in determining the most physically relevant modes, due to the absence of the ability to rank eigenvalue importance, unlike other ROM methods such as POD.[50]

In light of the limitations of POD and DMD, this work presents a novel method that combines both techniques, referred to as proper orthogonal decomposition (POD)–dynamic mode decomposition (DMD)–discrete Fourier transform (DFT) augmented analysis. This method effectively addresses the shortcomings of both methods while simultaneously revealing dynamic structures and elucidating the physical significance of the modes. Fu *et al.* successfully extracted the dominant flow structures within urban street canyons by employing the POD and DMD combining methods.[51] Based on our previous research, this article aims to employ the POD–DMD–DFT method to address the issue of how building gaps and interference impact airflow patterns and pollutant dispersion characteristics and elucidate the underlying mechanisms. Therefore, the purpose of the current study is as follows: (1) using LES to obtain the flow field data of traffic dispersion for different building cluster layouts; (2) employing the POD–DMD–DFT method to extract dominant flow structures and identify the influence of the modes on pollutant dispersion around building clusters; and (3) Finding the correlation between the building gaps and pollutant dispersion and proposing constructive strategies on urban planning.

The structure of this paper is as follows: Sec. II provides an introduction of the theory of POD, DMD, POD–DMD–DFT method, and details of LES simulation; Sec. III presents the research findings based on the innovative POD–DMD–DFT coupling analysis, and Sec. IV concludes the major findings.

II. METHODOLOGY

A. Proper orthogonal decomposition (POD)

The fundamental concept of POD is to determine the representation of a quantity based on an optimal orthogonal basis and the majority of the flow features can be represented by a few POD modes. The velocity components serve as the input while a set of orthogonal modes with corresponding time coefficients are generated as the output following the decomposition process. In this study, the fluctuating velocity serves as the flow field variable and is employed as the input for the POD process. A brief derivation is provided below.

$$u'(x, t_i) = \sum_{j=1}^{n} a_j(t_i)\phi_j(x), \tag{1}$$

where $u'(x, t_i)$ is the fluctuation velocity in matrix form, $\phi_j(x)$ is the POD mode, $a_j(t_i)$ is the temporal coefficient of the jth mode, n is the number of POD modes.

In our study, the spatial dimension greatly exceeds the temporal dimension, necessitating the snapshot POD method to identify POD modes due to the enormous size of the matrix $S = U^T U$, which renders the spatial POD method impractical for determining eigenfunctions. For POD analysis, the fluctuating velocity from LES can be represented by $X \times Y$ matrix, where X represents the number of grid points and Y is the time step number. S is the covariance matrix of $u'(x, t_i)$ of size $m \times m$, the eigenvalues are shared by S and the eigenvectors of these matrices can be related to each other

$$S\psi_j = \lambda_j \psi_j, \quad \psi_j \in \mathbb{R}^m. \tag{2}$$

Based on the fluctuating velocity data, the covariance matrix S can be calculated by solving its eigenvalue as follows:[52]

$$S\psi_j = \lambda_j \psi_j, \tag{3}$$

where λ_j is the eigenvalue representing the energy contribution of jth POD mode, ψ_j is the POD eigenvector, S is the covariance matrix of $u'(x, t_i)$ and defined as:

$$S = \sum_{i=1}^{n} u'^T(t_i) u'(t_i) = U^T U, \tag{4}$$

where the matrix U represents the m snapshot data being organized into a matrix format:

$$U = [u(t_1) \;\; u(t_2) \; \ldots \; u(t_m)] \in \mathbb{R}^{n \times m}. \tag{5}$$

After that, the POD mode $\phi_j(x)$ can be calculated based on eigenvectors and eigenvalues λ_j through

$$\phi_j = U\psi_j \frac{1}{\sqrt{\lambda_j}}. \tag{6}$$

B. Dynamic mode decomposition (DMD)

With its foundation in Koopman theory, DMD represents a linear approximation of intricate nonlinear dynamics.[44] The inputs of DMD consist of a sequence of snapshots derived from LES simulations at interval time Δt. The flow field data generated by numerical simulation can be represented as a sequence of snapshot, organized in the form of two snapshots in pair $(X_1{}^n, X_2{}^n)$ with a constant time interval:

$$X_1{}^n = \{x_1, x_2, x_3, \ldots, x_n\}, \tag{7}$$

$$X_2{}^n = \{x_2, x_3, x_4, \ldots, x_{n+1}\}, \tag{8}$$

where x_i represents for the ith flow field. The subscript 1 indicates the first number of the sequence, while the superscript n denotes the last element in the sequence. The constant sampling time between snapshots Δt is assumed and a linear operator A is employed to link the forward-step matrix x_i with the subsequent step matrix x_{i+1}:

$$x_{i+1} = Ax_i. \tag{9}$$

The subsequent sequence of flow field can be formulated as follows:

$$X_1{}^n = \{x_1, Ax_1, A^2x_1, \ldots, A^{n-1}x_1\}. \tag{10}$$

Then, the eigenvalues and eigenvectors of the linear operator A is calculated to represent DMD eigenvalues and modes. The linear operator A can be calculated by minimizing the Frobenius norm of $||X_{n+1} - AX_n||_F^2$. For large databases; however, it is typically not efficient to compute A precisely.[45] The whole rank A is approximated using a low-dimensional similarity matrix $\tilde{A}$

$$A = U\tilde{A}U^T, \tag{11}$$

where orthogonal square matrices contain the spatial information and the singular value decomposition (SVD) of $X_1{}^n$ is performed to compute linear operator A as:

$$X_1{}^n = U \sum V^T, \tag{12}$$

where orthogonal square matrices U and V^T contain the spatial and temporal information, respectively, and involve the information of the eigenvalue of POD mode.

By substituting Eqs. (11) and (12), $\tilde{A}$ can be an approximate representation of A and calculated by:

$$A \approx \tilde{A} = U^T X_2{}^n V \sum{}^{-1}. \tag{13}$$

The eigenvalue and eigenvectors of $\tilde{A}$ can be obtained through $\tilde{A}\varphi_i = \varphi_i y_i$, where φ_i and y_i are the eigenvector and eigenvalue matrix of DMD modes. Then, the DMD modes can be expressed by:

$$\Phi = X^{n+1} V \sum{}^{-1} \varphi_i, \tag{14}$$

where Φ is the DMD mode matrix. The real part of the eigenvalue of the DMD mode is associated with the mode growth/decay rate g_j while and imaginary part is associated with the mode frequency w_j, and can be expressed as:

$$g_j = Re\{\log(\mu_j)\}/\Delta t, \tag{15}$$

$$w_j = Im\{\log(\mu_j)\}/\Delta t, \tag{16}$$

where μ_j represents the eigenvalue of the jth DMD mode.

C. POD–DMD–DFT

The essence of POD lies in its capability to articulate the energy contribution of modes extending from the highest to the lowest frequencies. However, elucidating the correlation between dominant frequencies and specific flow patterns remains a formidable task within the realm of POD. In contrast to POD, Each DMD mode is associated with a distinct frequency, allowing for the exploration of flow field dynamics from a dynamic perspective. However, determining the physical relevance of DMD modes poses a challenge for researchers due to the lack of methods to rank the importance of eigenvalues associated with each mode. The application of POD and DMD for analyzing flow fields is confined to energetic or evolutionary perspectives, rendering it a daunting task for researchers to comprehensively elucidate the underlying mechanisms of air pollution dispersion from both aspects.

The POD–DMD–DFT method is introduced to address the limitations of POD and DMD mentioned in Sec. II A–II B, with the objective of assigning a unique frequency to each mode and establishing a hierarchical ranking for all modes based on the magnitude of eigenvalues. The POD–DMD–DFT process can be essentially categorized into three distinctive steps, as illustrated in Fig. 1. The first step involves applying both the POD and DMD methods to the flow field dataset

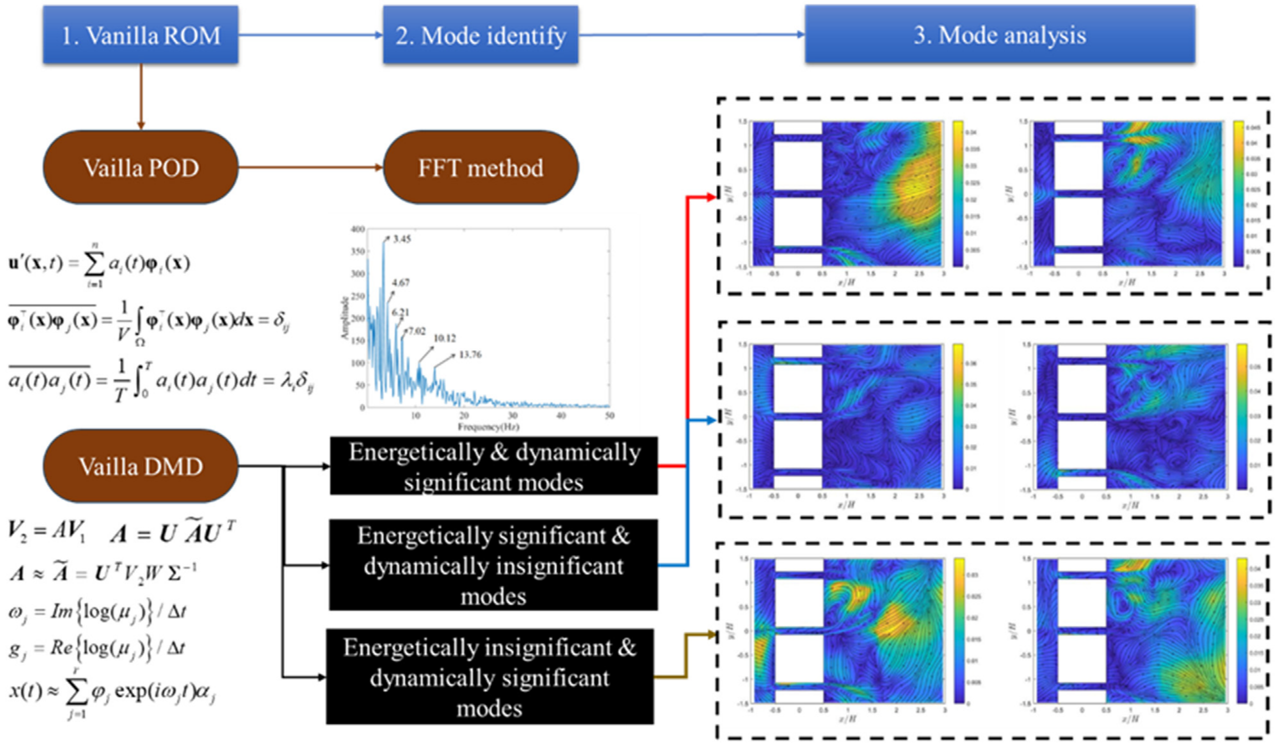

FIG. 1. POD–DMD–DFT analysis procedure.

derived from CFD simulations and the dominant frequency of the first POD mode is identified utilizing the fast Fourier transform (FFT) method. Subsequently, three types of modes can be categorized from energy and dynamic perspectives refer to Ref. 51. Modes that contribute the greatest energy to the whole flow field are defined as the energetically significant modes, while the modes that can continuously affect the evolution of the turbulence flow are called dynamically significant modes. The classification is as follows: (1) Type 1: Energetically and dynamically significant mode, a high-order DMD mode that possesses the dominant frequencies of the primary POD modes. (2) Type 2: Energetically significant and dynamically insignificant mode, a lower-ranked DMD mode that possesses the dominant frequencies of the primary POD modes. (3) Type 3: Energetically insignificant and dynamically significant mode, a higher-order DMD mode that owns the dominant frequencies of the low-ranking POD modes. Then, the mode contribution will be evaluated in accordance with the respective mode patterns of each mode type with respect to three building layouts.

D. Computational settings and parameters of LES

This work is the extensive study of isolated-building scenarios, with the precision of the LES model utilized in this investigation being enhanced through rigorous validation of the isolated-building model. The comprehensive validation work for the isolated-building model has been included in the Appendix. Isolated building numerical validation as a reference for relevant researchers and will not be reiterated here.

1. Building array model and computational domains

Figure 2 demonstrates the configuration of building array models with different building widths (*B*) and the distance between the two buildings (*S*). Rectangular buildings with an aspect ratio [height (*H*)/width (*B*)] of 5:1 have been chosen to represent the most aerodynamic characteristics of high-rise buildings.[53] The dimensions of each building are 100 × 100 × 500 mm^3 [depth (*D*) × width (*B*) × height (*H*)]. The building array model was composed of six buildings in tandem arrangement with different wind corridor widths. Three different building group layouts were defined based on different passage widths, namely Type-a layout ($S/B=1$), Type-b layout ($S/B=0.05$), and Type-c layout ($S/B=1$ and $S/B=0.05$). Type-c layout was a combination of Type-a and Type-b layout, in which six buildings were divided into three groups. The introduction of building gaps, also referred to as wind corridors, has been proposed as a potential solution for mitigating the wall effect and is the primary research parameter in this research. This investigation systematically examines the impact of varying gap widths (*S*) ranging from 0.05 *B* to 1 *B*, representing high-density cities such as Hong Kong and other Asian cities.[53] The distance between each building group equals the *S*/*B* in the Type-a layout while the distance between each building within one group equals the *S*/*B* in the Type-b layout.

The configuration of the computational model for three building array models is illustrated in Fig. 3. The tracer gas was emitted from a linear source located at the ground level, 0.1 *H* away from the leeward wall of the building array, as shown in Fig. 3. The computational domain inlet, laterals, and outlet were 4*H*, 3*H*, and 10*H* away from the

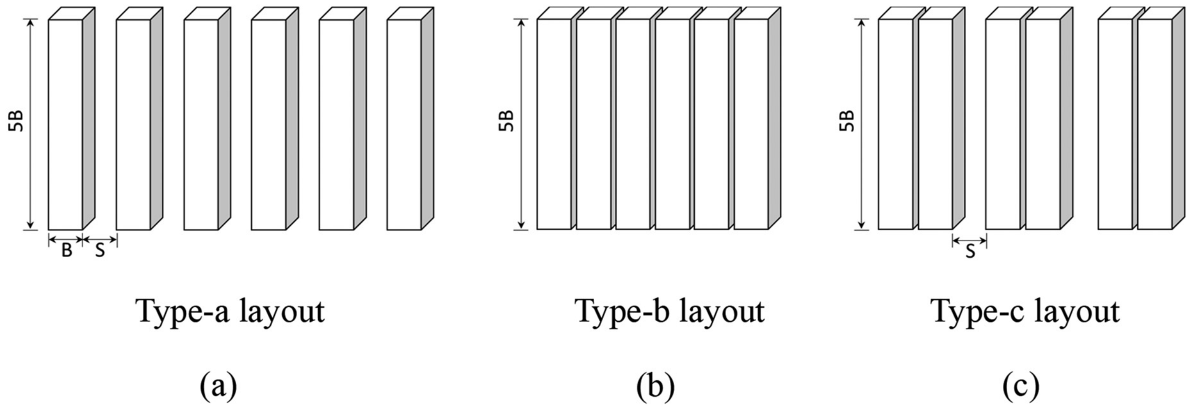

FIG. 2. Test building configurations for (a) Type-a layout ($S/B = 1$), (b) Type-b layout ($S/B = 0.05$), and (c) Type-c layout ($S/B = 1$ and 0.05).

building models' boundary. The height of the CFD region is $6H$. The computational domain size is aligned with the AIJ Guideline[54] and is sufficiently large enough to avoid the potential boundary effect between the building and the lateral wall.

2. Mesh generation and Boundary condition settings

The whole mesh domain is divided into two subdomains, the fine inner domain Ω_1, and the coarse outer domain Ω_2 to meet the balance between low computational cost and high simulation accuracy. The inner domain Ω_1 is extended from the boundary of the buildings to $1H$ away from the array of buildings with the non-dimensional hexahedral mesh size $\Delta L/H = 0.001$. At the transient area between Ω_1 and Ω_2, a mesh refinement ratio is 1.2 for the smooth transition from the inner to the outer region. In the outer domain Ω_2, the stretching ratio of adjacent cells was 1.05. The total number of cells is 11.9×10^6, 11.7×10^6, and 12.9×10^6 for three cases, respectively. The average non-dimensional distance y^+ of the first near-wall grids is below 1 and the first cell height from the adjacent wall is 6.765×10^{-5} m.

For the boundary conditions, the no-slip wall condition was adopted for the ground surface of the building, and the domain ceiling and laterals were set as symmetry boundary conditions to replicate the ceiling, ground, side walls, and building surfaces in the wind tunnel experiment. The outlet boundary condition was set as the outlet with zero static pressure. The building Reynold number, which is determined by H (0.5 m) and U_{ref} (5 m/s), is 1.7×10^5. The atmosphere boundary layer (ABL) profile including velocity, turbulent kinetic energy (TKE), and turbulent dissipation equation follows the derivation proposed by Richards and Hoxey[55] as follows:

$$u = \frac{u^*}{\kappa} ln\left(\frac{z + z_0}{z_0}\right), \tag{17}$$

$$k = \frac{u^{*2}}{\sqrt{C_\mu}}, \tag{18}$$

$$\varepsilon(z) = \frac{u^{*3}}{\kappa(z + z_0)}, \tag{19}$$

where u^* is the ABL friction velocity, z_0 is the roughness length, and κ is the Von Karman constant, C_μ is the model constant set as 0.09, and z is the height along z-axis. z-axis refers to the vertical direction. The determination of u^* and z_0 is by logarithmic law curve fitting the mean wind velocity profile of wind tunnel experiment data from Gromke *et al.*,[56] which is 0.59 m/s and 0.004 m.

3. LES model, solver settings, and sampling statistics

All cases were computed using ANSYS Fluent, and the Smagorinsky model[52] with Lilly formulation has been adopted in the current study to further model the transient flow fields.[57] In the LES, the following grid-filtered operation filters the governing equations of unstable 3D incompressible flow:

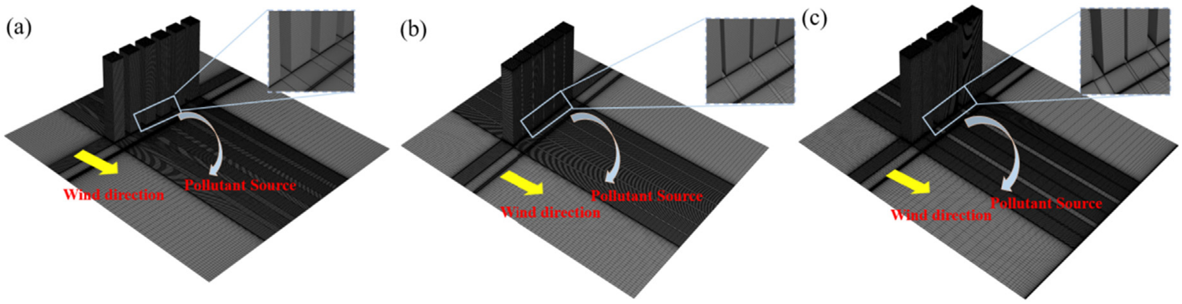

FIG. 3. Configurations of (a) Type-a layout, (b) Type-b layout, and (c) Type-c layout.

$$\frac{\partial \overline{u_i}}{\partial x_i} = 0, \tag{20}$$

$$\frac{\partial \overline{u_i}}{\partial t} + \overline{u_j}\frac{\partial \overline{u_i}}{\partial x_j} = -\frac{1}{\rho}\frac{\partial \overline{p}}{\partial x_i} - \frac{\partial \tau_{ij}}{\partial x_j} + \upsilon\frac{\partial^2 \overline{u_i}}{\partial x_j^2}, \tag{21}$$

$$\tau_{ij} = \overline{u_i u_j} - \overline{u_i}\,\overline{u_j}, \tag{22}$$

$$\overline{S_{ij}} = \frac{1}{2}\left(\frac{\partial \overline{u_i}}{\partial x_j} + \frac{\partial \overline{u_j}}{\partial x_i}\right), \tag{23}$$

where $\overline{u_i}$ is the component of the filtered velocity in the ith direction and $\overline{u_j}$ is the component of the filtered velocity in the jth direction, $\overline{p}$ is the filtered pressure, ρ is the density, $\overline{S_{ij}}$ is strain rate tensor, tilde represents spatial filtering by a 3D filter of size Δ, τ_{ij} is the subgrid-scale model stress tensor.

The eddy viscosity υ_T in the Smagorinsky model is defined as the following equation[52] connecting the subgrid stress to the filtered rate of strain $\overline{S_{ij}}$:

$$\upsilon_T = [C_S\Delta]^2|\sqrt{2\overline{S_{ij}}\,\overline{S_{ij}}}, \tag{24}$$

where C_S is the Smagorinsky constant, Δ is the filter width. In this study, $\Delta = V_{cell}^{1/3}$ is adopted for a grid-dependent filer in the physical space, V_{cell} is the cell volume.

The methods proposed by Werner and Wengle[58] have been adopted for near-wall treatment in Ansys Fluent. The wall shear stress was computed considering the power-law near-wall velocity distribution in the following expressions:

$$|\tau_w| = \begin{cases} \dfrac{2\mu|u_p|}{\Delta z} \\ \quad \text{for} \quad |u_p| \le \dfrac{\mu}{2\rho\Delta z}A^{\frac{2}{1-B}}, \\ \rho\left[\dfrac{1-B}{2}A^{\frac{1+B}{1-B}}\left(\dfrac{\mu}{\rho\Delta z}\right)^{1+B} + \dfrac{1+B}{A}\left(\dfrac{\mu}{\rho\Delta z}\right)^{B}|u_p|\right]^{\frac{2}{1+B}} \\ \quad \text{for}\ |u_p| > \dfrac{\mu}{2\rho\Delta z}A^{\frac{2}{1-B}}, \end{cases} \tag{25}$$

where μ is the air dynamic viscosity, ρ is the air density, Δz is the vertical size of the cell volume next to the wall. A and B are parameters set as 8.3 and 1.7, respectively. u_p is the instantaneous velocity components tangential to the wall, τ_w is the instantaneous wall-shear stress.

The finite volume approach was used to discretize the governing equations for isothermal incompressible flows. Both the RANS and the LES models were used in the simulation process. First, a steady RANS simulation was employed to obtain steady flow fields, preparing initial conditions for LES simulations. The pressure implicit with splitting of operators (PISO) algorithm has been applied in LES with respect to solver settings. The non-iterative time advancement (NITA) pressure–velocity coupling scheme is incorporated into the simulation. The second-order implicit formulation was employed for temporal terms. A fully turbulent wind flow at the inlet is simulated by the spectral synthesizer method. Therefore, $\Delta t = 1.5 \times 10^{-4}$ s and the LES simulations are continued for an additional 6 s to gather the data once the solution has fully converged. The simulation started at 6 s (40 000 time steps), and stop time is 12 s (80 000 time steps). The temporal interval between consecutive files is 0.01 s. The literation computation was considered to reach a convergence when all residual curves approximately stayed stable and residuals for continuity, momentum, and turbulence were below 10^{-4} for convergence. The Courant–Friedrichs–Lewy (CFL) condition of less than 1 was satisfied.[59,60]

The accuracy of the data from LES simulation lays the groundwork for POD and DMD analysis. The data should be confirmed to be statistically steady due to the instantaneous velocity and the fluctuation of turbulent flow. On this basis, two monitoring points in front (0.1H, 0, 0.5H) and behind (−0.1H, 0, 0.5H) the building array has been set to make sure the value is stationary in LES simulation, as shown in Fig. 4(a). The normalized wind velocity shows obvious fluctuations in the initial time steps, while the data converges and become stationary after 40 000 time steps. The data after the 40 000 time steps were chosen and sampled for future POD and DMD analysis.

In order to further confirm the accuracy of LES, an 80% resolution for the TKE between the energy-containing range and the inertial subrange should be obtained.[61] The quantitative index $LESIQ_v$ proposed by Calik *et al.*[62] was utilized to ensure the accuracy of LES as follows:

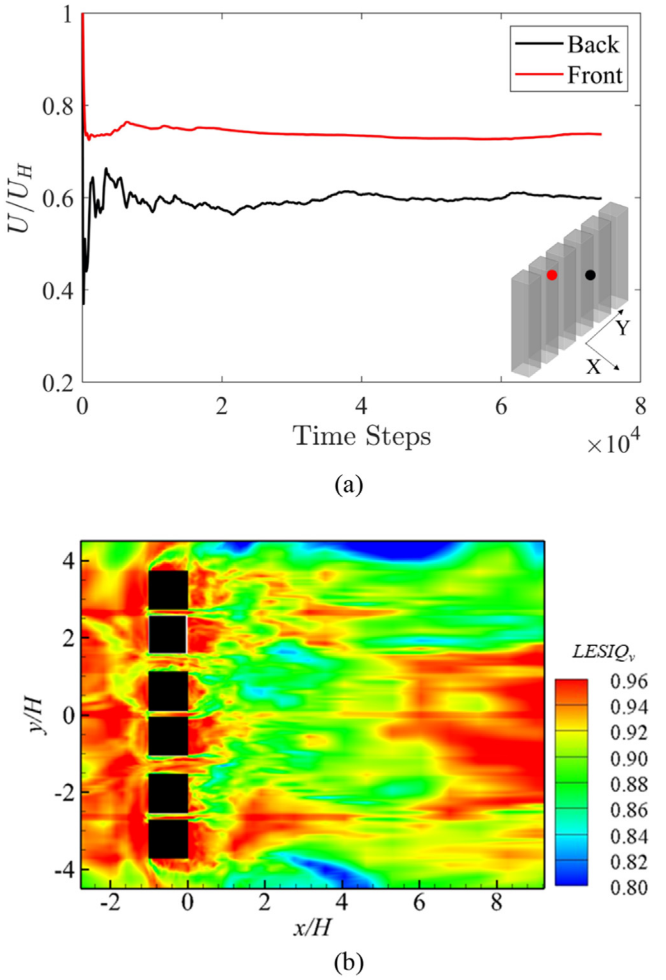

(a)

(b)

FIG. 4. (a) Convergence monitoring for normalized wind velocity for two monitoring points and (b) $LESIQ_v$ contour of the pedestrian level plane.

$$LESIQ_{\upsilon} = \frac{1}{1 + 0.05\left[\dfrac{\upsilon + \upsilon_{sgs}}{\upsilon}\right]^{0.53}}. \tag{26}$$

Here, υ denotes the fluid molecular kinematic viscosity, and the greater the $LESIQ_v$, the better the grid resolution. Typically, an index $LESIQ_v$ exceeding 80% denotes an appropriate grid resolution. The $LESIQ_v$ contour at the pedestrian level is depicted in Fig. 4(b). It shows the resolution is over 80% within the whole area and the quality of grid resolution is confirmed by $LESIQ_v$, which reaches over 85% for most of the area.

III. RESULTS AND DISCUSSION

A. Mean wind velocity analysis

The presence of bluff bodies in a flowing viscous fluid typically induces changes in the trajectory of the incoming flow due to drag effects. In this section, the effect of building layout on mean flow regimes will be discussed. The height of the plane is $z = 0.01$ m, representing the height at pedestrian level in the scaled-down model and 2 m in the prototype. Figure 5 displays normalized pedestrian-level mean wind velocity $\overline{U}/U_{ref}$ distributions surrounding three different building layouts. U_{ref} denotes the reference velocity at the height of the buildings, which is 4.94 m/s in this study. The array of buildings exhibits a notable wind-resistance influence on the incoming airflow, leading to the development of a relatively stagnant region with diminished wind speed in front of the building arrays. The flow patterns within the passages between buildings exhibit an acceleration phenomenon, which can be attributed to the Venturi effect which describes an inverse relationship between flow velocity and cross-sectional area.[63] Lateral high-velocity regions can be observed within the building array where the corner stream is situated.

For the Type-a layout [as depicted in Fig. 5(a)], the vortices generated behind each building are mutually independent, and the interaction between them remains unobservable due to the relatively wide spacing between buildings. The maintenance of a consistently high velocity of pollutant dispersion along the street is observed when the distance between each building exceeds the width of the recirculation region. For the Type-b layout [Fig. 5(b)], the closely positioned

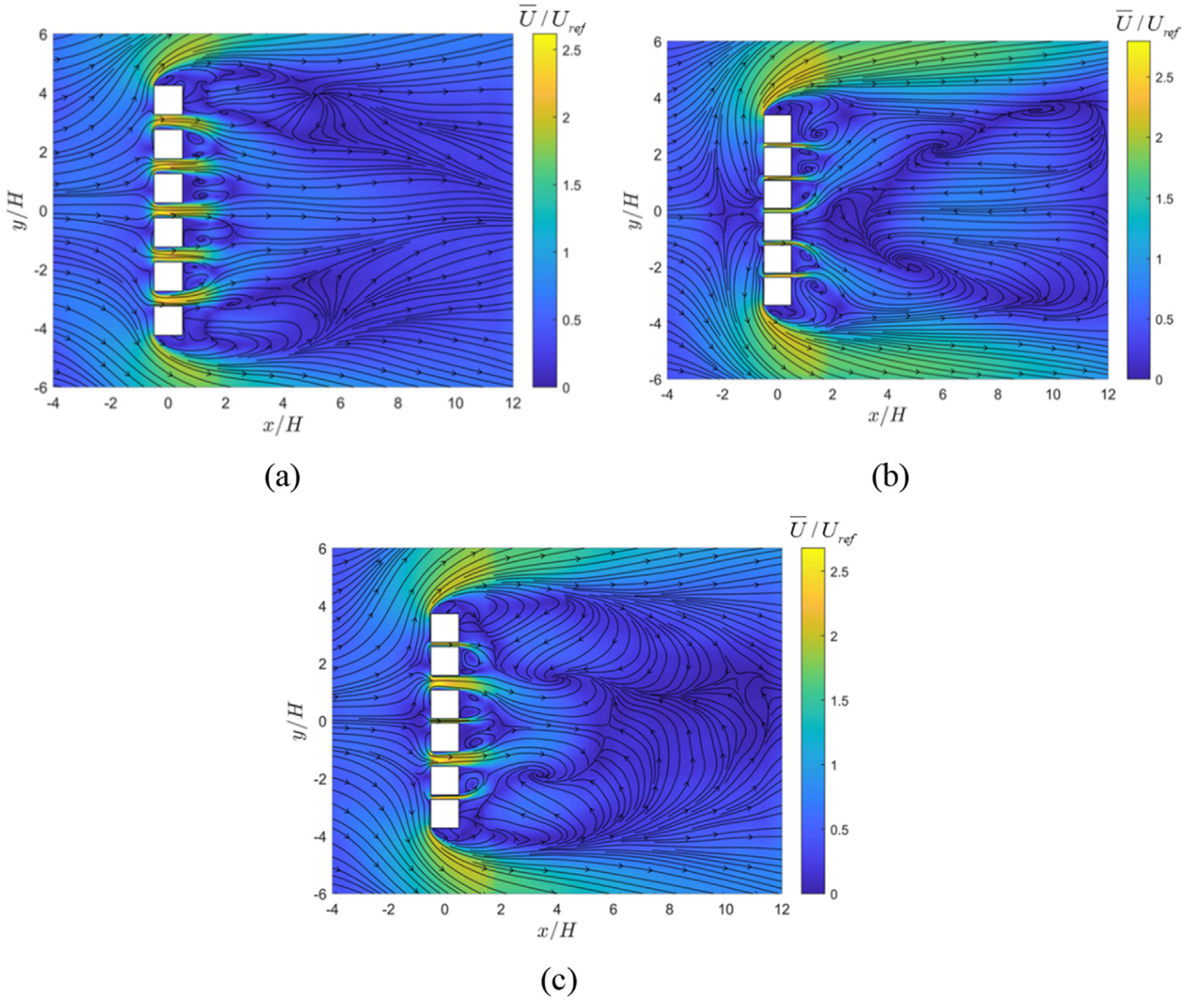

(a)

(b)

(c)

FIG. 5. Normalized mean wind velocity $\overline{U}/U_{ref}$ contour for (a) Type-a layout, (b) Type-b layout, and (c) Type-c layout at pedestrian level.

buildings enhance the turbulent flow regime and amplify the interaction between vortices formed behind each structure, thereby accentuating the absence of recirculation for buildings situated in the middle of the array. Similar phenomena are also reported in the literature,[64] the turbulent dispersion effect dominates the advection of pollutants in narrow streets, leading to their accumulation in recirculation regions. With respect to the flow regime surrounding the Type-c layout [Fig. 5(c)], the shedding effects of high-rise buildings result in a significant proportion of airflow being redirected over the passage rather than through it, thereby enhancing the complexity of predicting wind velocities within the inter-building corridor. Moreover, the generation of three pairs of vortices consecutively behind each cluster of buildings is observed. At the passages connecting these building clusters, similar to the Type-a layout, a significant improvement in pollutant removal efficiency is noted due to the presence of high-velocity flow extending toward the far end. Thus, by appropriately adjusting the spacing between buildings in urban areas, it becomes feasible to achieve an acceptable solution for pollutant accumulation.

B. POD analysis

1. POD mode identification

The three-dimensional sample data are utilized for both the analysis of proper orthogonal decomposition (POD) and dynamic mode decomposition (DMD), as well as serving as the computational domain for large eddy simulation (LES). For subsequent POD and DMD analyses, the input data consisted of three-dimensional flow field component snapshots. To provide readers with a more comprehensive perspective, two-dimensional flow visualization at the pedestrian-level height plane is presented in the Secs. III A–III C. The proper orthogonal decomposition (POD) method is extensively employed in the fields of turbulence and fluid dynamics to extract coherent structures from turbulent flows. The mean-subtracted fluctuating field serves as the input for POD to identify the dominant features in various configurations. The convergence of POD analysis is confirmed by examining the reconstruction accuracy of POD models using the mean l_2-norm of reconstruction error.[65] The convergence of POD analysis is confirmed by examining the reconstruction accuracy of POD modes using the mean l_2-norm reconstruction error as follows:

$$\|e\|_{2,ins} = \frac{1}{n}\sum_{k=1}^{n}\left[\left(\frac{x_{rec,k,i}-x_{k,i}}{x_{k,i}}\right)^{2}\right]^{\frac{1}{2}}, \qquad (27)$$

where $x_{rec,k,i}$ denotes the reconstructed data at node k and instant i, $x_{k,i}$ is the original data. Figure 6 illustrates the reconstruction error and time for different mode numbers. When the number of selected modes exceeds 500, the error decreases and the discrepancy between the 500-model and full model remains within an acceptable range, indicating that the remaining POD modes contribute insignificantly to the flow field. This suggests that flow field reconstruction reaches a state of independence.

When sample data exceeds 500 POD modes, the reconstruction accuracy remains nearly invariant, indicating independence from sampling. Therefore, for the data employed in POD and DMD analysis, a total of 500 POD modes are generated. Figure 7 depicts the cumulative energy contributions of POD modes for three different building layouts. The analysis indicates that 500 POD modes account for over 98% of the total energy, with dominant modes exhibiting the highest energy proportion and a steep decline in contribution observed for higher-order modes. The dominant mode accounts for approximately 10% of the total energy for all three cases. Due to the pronounced three-dimensional turbulence effect at pedestrian height, the flow information in the plane fails to fully capture all flow characteristics. Consequently, when compared to quasi-two-dimensional flows exhibiting high spanwise correlation, the model energy accumulation resulting from POD decomposition is comparatively reduced. The cumulative energy proportion from the first two modes is 15.2%, 23.8%, and 20.4% for each of the three building layouts, respectively. Convergence is observed when selecting more than 50 POD modes. In order to elucidate the dominant mechanism of fluctuating wind fields, the first two modes with the highest energy contribution have been chosen.

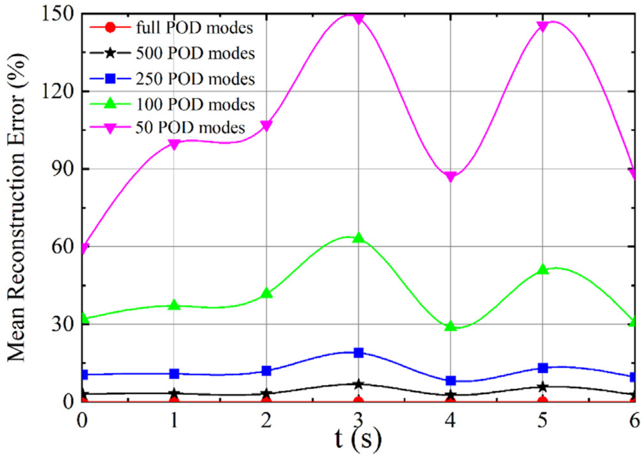

FIG. 6. The reconstruction error with time for different POD models involved.

2. Dominant POD modes pattern for different building layouts

The first two POD modes with normalized velocity on the pedestrian-level plane at $z = 0.01$ m with respect to Type-a layout are shown in Fig. 8, together with dominating frequencies determined by FFT analysis based on the time coefficient of the mode. The flow pattern of POD mode 1 is shown in Fig. 8(a), which contains 7% of the total energy. The presence of two symmetrical vortices behind the central buildings can be attributed to the flow recirculation phenomenon occurring in close proximity to the wake region. The location of flow reattachment is $3H$ downstream of the building arrays. As illustrated in Fig. 8(c), the dominant frequency of POD mode 1 is 3.45 Hz. In contrast, the POD mode 2 pattern shown in Fig. 8(b) features vortices with much smaller scales than those in mode 1, which predominantly contribute to the formation of the small vortices in the mean wind flow field. The flow attachment point is located at $1H$, which is shorter than the length of the recirculation region of mode 1.

Figure 9 demonstrates the first two node patterns and corresponding FFT results with respect to the Type-b layout. A diminutive vortex is detected behind the buildings in the POD mode 1, in

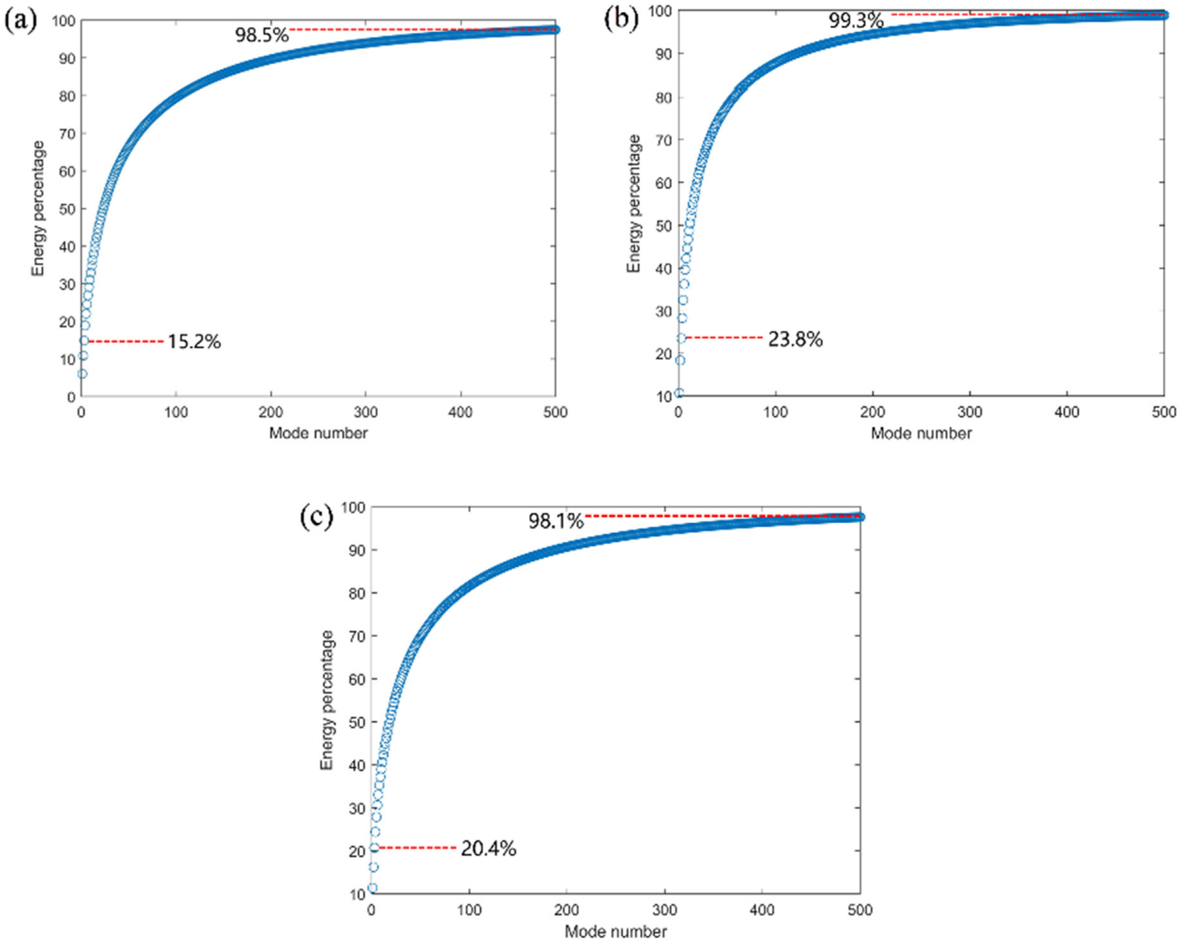

FIG. 7. Energy contribution of POD modes with respect to (a) case type-1, (b) case type-2, and (c) case type-3.

comparison to the Type-a layout due to the constricted passages between buildings as shown in Fig. 9(a). The position of flow reattachment is closer to the buildings in comparison to the Type-a layout, declining to 1.5 H behind the building. Moreover, in contrast to the symmetric vortex pattern in the Type-a layout, only one vortex at $x/H = 1$ is formed in POD mode 1 and mode 2, as shown in Figs. 9(a) and 9(b). A constricted wind passage may undermine the integrity of the Karman vortex, leading to an asymmetry in vortex structures behind buildings. As depicted in Figs. 9(c) and 9(d), the dominant frequency of mode 1 and mode 2 is significantly smaller compared to that in the Type-a layout. The attenuation of building passage width will augment the preponderant impact of the first two POD modes on the dynamic flow field, thereby inducing a more discernible effect.

Figure 10 illustrates the first two POD mode patterns at pedestrian-level height with the dominant frequencies' information from FFT analysis. The primary POD mode 1 pattern encompasses the flow characteristics manifested by both Type-a and Type-b layouts. For POD mode 1 [as depicted in Fig. 10(a)], it exhibits two symmetrically positioned vortices behind the buildings, resembling the POD mode 1 pattern of Type-a [Fig. 8(a)]. The scale of these vortices is commensurate with that observed in the Type-b layout [Fig. 9(a)], which is noticeably smaller than the Type-a layout.

Furthermore, the dominant frequency magnitudes of the first two modes fall within the range between Type-a and Type-b layouts. In POD mode 2, smaller vortices arise behind the array of buildings, with a notably diminished distance between these vortices and the leeward side of the buildings compared to those observed in POD mode 2 for Type-a layout.

The dominant patterns of POD modes can be utilized to visualize the coherent structures in turbulent flows. Nonetheless, each POD mode typically exhibits multiple dominant frequencies resulting from the non-orthogonality and entanglement, as revealed by FFT. The POD analysis fails to establish a correlation between the dominant frequencies and specific flow patterns, rendering it insufficient for exploring the dynamic aspects of pollutant behavior solely based on POD analysis. Consequently, it is imperative to perform DMD analysis on the identical dataset in order to accurately determine the flow pattern associated with each dominant frequency.

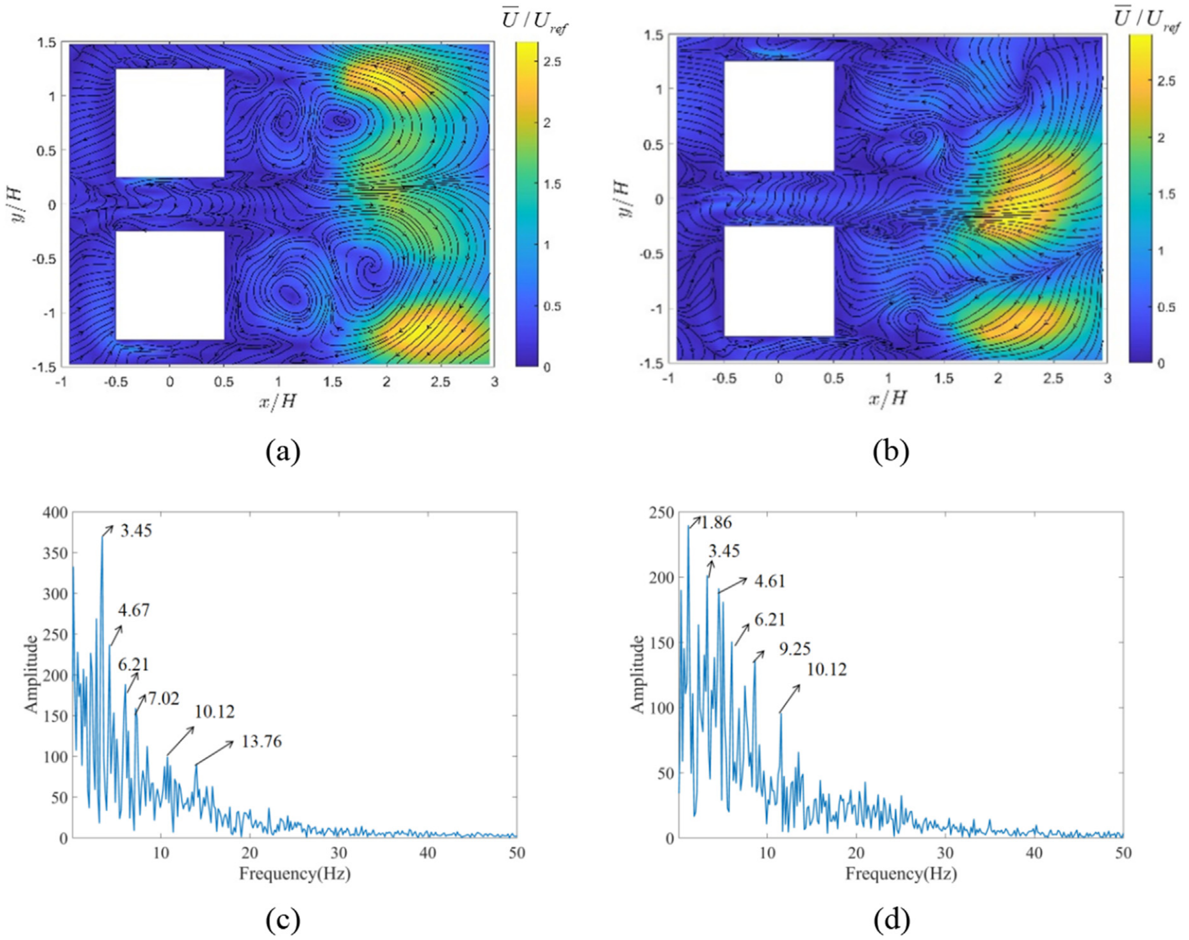

(a) (b)

(c) (d)

FIG. 8. Normalized velocity vectors on the pedestrian level plane at $z = 0.01$ m of (a) POD mode 1, (b) POD mode 2, and FFT results based on POD mode's coefficients: (c) POD mode 1 and (d) POD mode 2 in Type-a layout.

3. DMD analysis

The DMD modes are ranked according to the α-criterion proposed by Kutz *et al.*[48] which correlates the significant model contribution with model amplitude. The mean l_2-norm reconstruction error is calculated for different DMD modes using Eq. (27) and presented in Fig. 11. Similar to POD reconstruction models, when the number of DMD modes exceeds 500, the reconstruction error stabilizes and becomes independent of the mode number, indicating accurate results. Therefore, 500 DMD modes are considered in the following analysis.

The 500 DMD modes generated in this study are sorted in descending order of their modal amplitude to identify the dominant mode. The first two nodes with the highest amplitudes are regarded as the dominant DMD modes with respect to different building layouts. The growth/decay rate and mode frequency are determined by the DMD eigenvalue. The eigenvalues on the unit circle indicate that the relevant dynamic structures are undergoing stable oscillations.[66] In this study, the location of all DMD modes on the unit circle signifies mode stability.

In this study, the location of all DMD modes on the unit circle signifies mode stability, as shown in Fig. 12.

The grand mean error vs the sampling cycles based on the Eq. (27) is depicted in Fig. 13, where it can be observed that for sampling cycles higher than 45, the grand mean error remains nearly invariant, thereby ensuring the accuracy of DMD analysis from a convergence perspective.

The oscillatory DMD modes generate a pair of conjugate modes, where each component corresponds to either a real or imaginary conjugate of an eigenfrequency. The oscillatory DMD mode comprises two components with positive or negative physical frequencies and real or imaginary mode shapes while maintaining identical growth rates and modal contributions. Hence, the modes are presented in a paired manner to extract coherent flow mechanisms, as DMD modes are paired as complex conjugates. Figure 14 describes the normalized velocity at the pedestrian-level plane of the first two pairs of DMD modes with respect to the Type-a layout. As depicted in Fig. 14(a), the DMD mode 1–2 determines the formation of two large symmetric vortices downstream of the building, which constitutes the primary flow

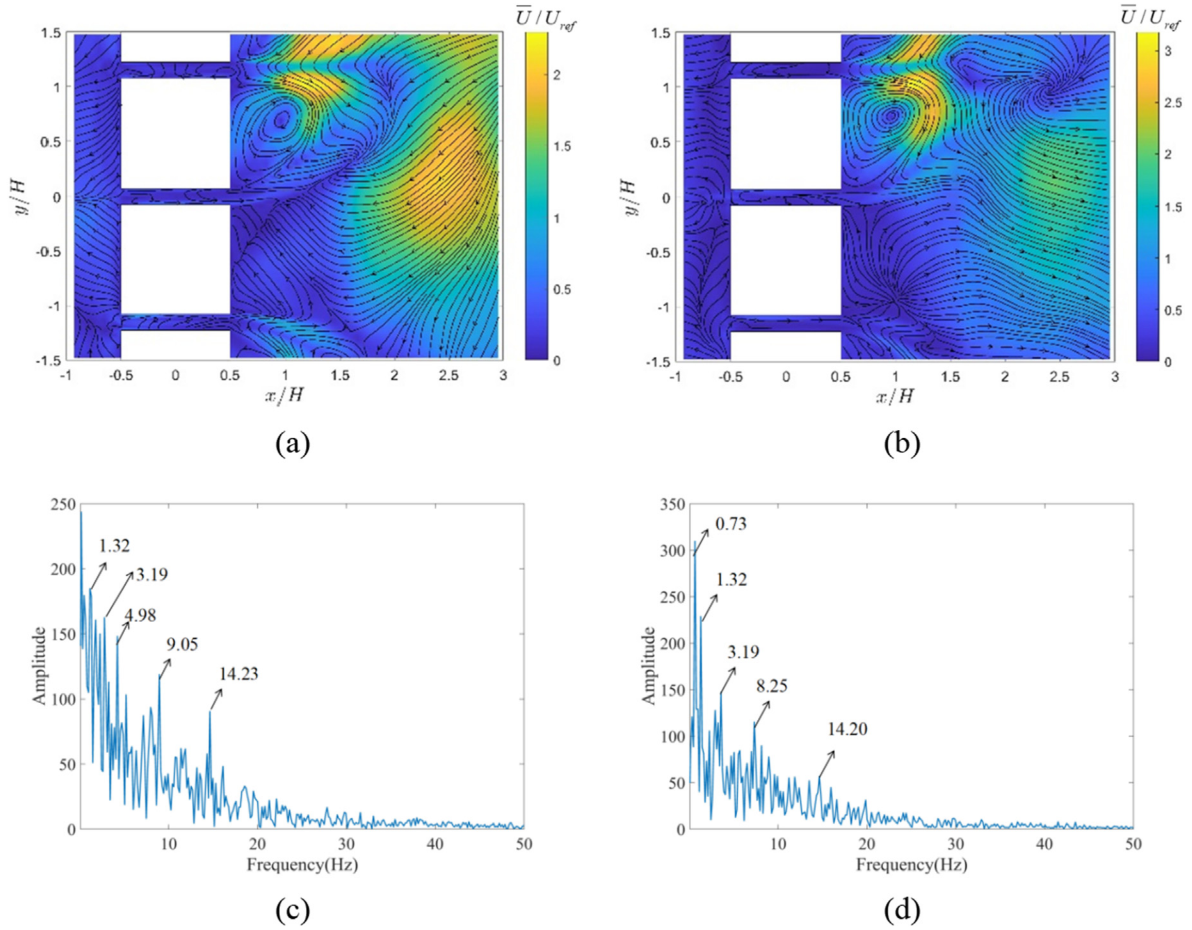

FIG. 9. Normalized velocity vectors on the pedestrian level plane at $z = 0.01$ m of (a) POD mode 1, (b) POD mode 2, and FFT results based on POD mode's coefficients: (c) POD mode 1 and (d) POD mode 2 in Type-b layout.

field structure. For the DMD mode 3–4 [Fig. 14(b)], the presence of a pronounced velocity gradient is observed at the termination of the recirculation region, concurrently giving rise to a pair of smaller vortices, which are situated 1.25*H* downstream within the wake region.

Figure 15 shows the first two dominant mode patterns with respect to the Type-b layout, which are DMD mode 1–2 with a mode frequency of 1.32 Hz [Fig. 15(a)], and DMD mode 3–4 with a mode frequency of 3.19 Hz [Fig. 15(b)]. The upstream buildings' sheltering effect leads to notable disruptions in the flow field posterior to the structure. Consequently, both vortex size and intensity are diminished in comparison to the Type-a layout. Furthermore, symmetrical vortex patterns are absent, and the recirculation area is the smallest among all three building layouts. A series of undeveloped and disordered vortices can be identified behind the structure.

The first two dominant modes pattern with respect to Type-c layout is portrayed in Fig. 16. Two dominant DMD modes are mode 1–2 with a mode frequency of 1.32 Hz [Fig. 16(a)], and DMD mode 3–4 with a mode frequency of 3.19 Hz [Fig. 16(b)]. The dominant frequencies of the first two DMD modes in Type-a layout exhibited a significant decrease, from 3.45 to 0.85 Hz and from 4.67 to 1.44 Hz, signifying a robust correlation between the dominant DMD mode frequency and building layouts. In DMD mode 1–2, two vortices with diminished intensity appear in the vicinity of the building, resulting in a smaller scale of vortex compared to the Type-a layout. This leads to a shorter recirculation region for the Type-c case. For DMD mode 3–4, the vortex appears at the same location with identical length as observed in mode 1–2. Moreover, in this mode pair, the single vortex behind each building decomposes into a symmetrical vortex pair, indicating that the scale of the vortex decreases as the mode frequency increases.

However, the vanilla DMD analysis lacks a technique to rank the importance of eigenvalues, which is crucial for determining energy significance when considering the velocity field. This limitation persists despite the fact that the DMD mode identifies dynamic structures associated with characteristic frequencies. Consequently, in order to address this issue, an analysis combining POD and DMD (referred to as POD–DMD–DFT augmented analysis)[51] is applied and discussed in Sec. III C.

C. POD–DMD–DFT augmented analysis

1. POD–DMD–DFT augmented mode classification

The field of fluid mechanics has increasingly focused on exploring the similarities and differences between proper orthogonal

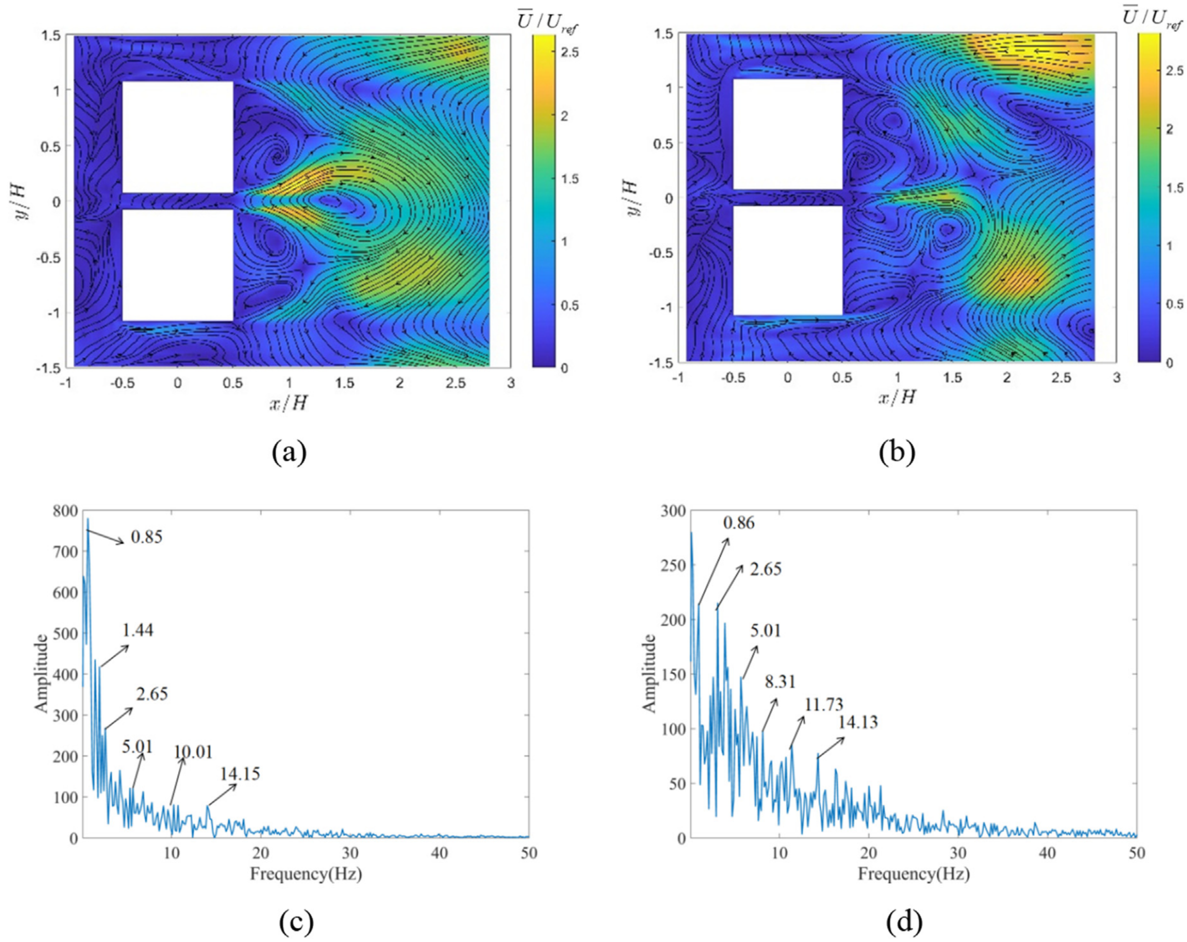

FIG. 10. Normalized velocity vectors on the pedestrian level plane at $z = 0.01$ m of (a) POD mode 1, (b) POD mode 2, and FFT results based on POD mode's coefficients: (c) POD mode 1 and (d) POD mode 2 in Type-c layout.

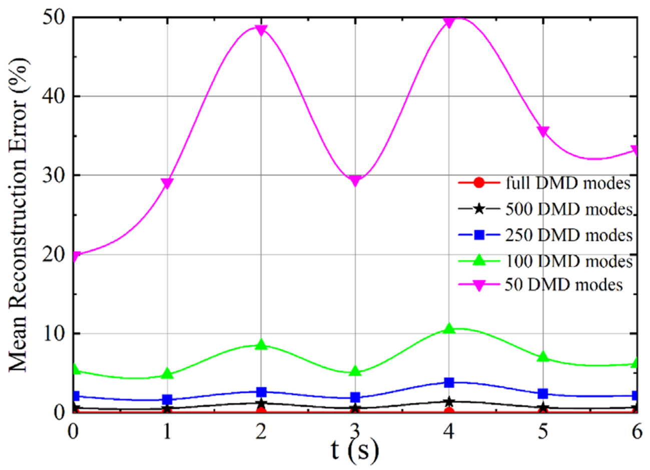

FIG. 11. The reconstruction error with time for different DMD models involved.

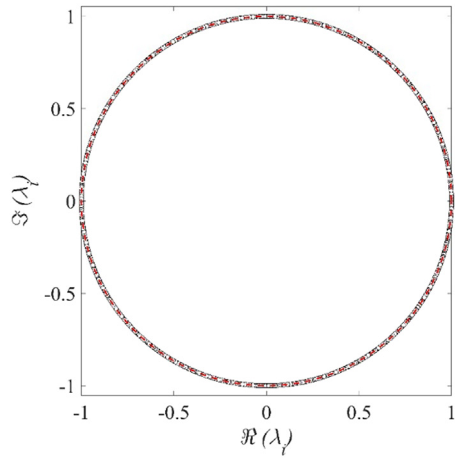

FIG. 12. DMD spectrum.

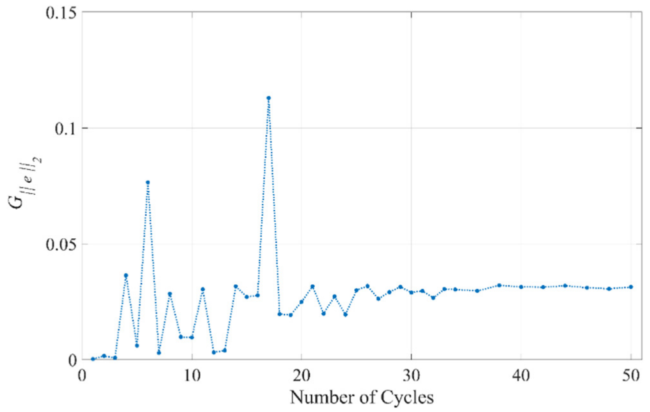

FIG. 13. Variation of grand mean error with the number of sampling cycles in the present study.

decomposition (POD) and dynamic mode decomposition (DMD). Zhang *et al.* discovered that while POD modes often contain irrelevant structures, each structure mode identified by DMD possesses distinct physical interpretations in terms of both spatial distribution and temporal behavior.[66] Both the POD and DMD methods are limited to offering a single perspective when examining dispersion issues within urban layouts, individually emphasizing solely the energetic and evolutionary aspects, respectively. It is inadequate for researchers to comprehensively explore the pollutant diffusion mechanisms. The POD–DMD–DFT augmented analysis is capable of assigning a distinct frequency to each decomposed mode and ranking all modes according to their significance in terms of eigenvalues. The detailed mode classification and POD–DMD–DFT augmented analysis procedure are in Sec. II C.

The Type-2 modes, characterized by their high-order nature and relatively low dominant frequency, are modes that have a limited impact on energy perspectives. They may, however, facilitate sudden pollutant transport in the wake region. In contrast, Type-3 modes, characterized by their low mode order and high mode frequency, define flow patterns that are less dominant but persistent in the long term. Consequently, the contribution of the Type-3 mode is primarily from a dynamic perspective.

Table I describes the DMD modes belonging to the three types of modes for different building layouts. A distinct correlation between the mode type and dominant frequency can be observed, with Mode Type-1 consistently associated with lower frequencies across all three building layouts. A diminutive frequency signifies a consistent process of contribution, whereas a decreased mode order suggests that these modes are the principal energy contributors to the mean flow field. Consequently, these modes are predominantly influenced by both energy and dynamic aspects. The Type-2 modes, characterized by their high-order nature and relatively low dominant frequency, are modes that have a limited impact on energy perspectives. They may, however, facilitate sudden pollutant transport in the wake region. In contrast, Type-3 modes, characterized by their low mode order and high mode frequency, define flow patterns that are less dominant but persistent in the long term. Consequently, the contribution of the Type-3 mode is primarily from a dynamic perspective.

2. Analysis of Type-1 POD–DMD–DFT mode for three building layouts

Type 1 mode has been defined as the energetically and dynamically significant mode, the Type 1 mode patterns with respect to three building layouts are demonstrated in Fig. 17. These dominant modes play an important role in determining the turbulence flow field characteristics from both energy and dynamic perspectives and describe the dominant flow structures of the flow field. The first two modes associated with specific phenomena are selected for presentation here due to their significant energy contribution. The first mode corresponds to the presence of symmetrical vortices behind the building clusters, while the second mode is responsible for generating smaller vortices characterized by a pronounced velocity gradient. The POD–DMD–DFT mode corresponding to Type 1 serves as the primary energy contributor, facilitating the continuous conveyance of energy to the mean flow field. The scale of vortex pairs in Type 1 mode decreases as buildings approach, which is also evident in the original mean flow field. The

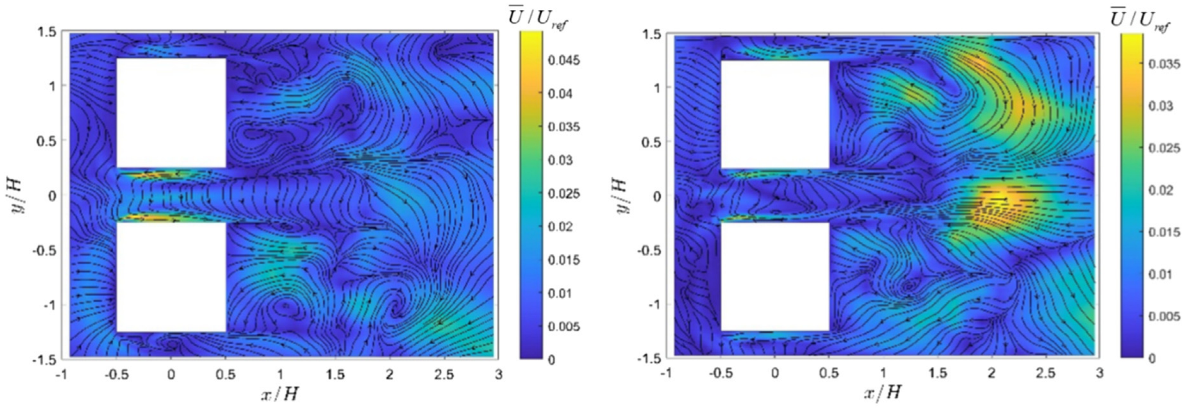

(a) DMD mode 1-2 (3.45 Hz)

(b) DMD mode 3-4 (4.67 Hz)

FIG. 14. Normalized velocity vectors on the pedestrian-level plane at $z = 0.01$ m of (a) DMD mode 1–2 and (b) DMD mode 3–4 with respect to Type-a layout.

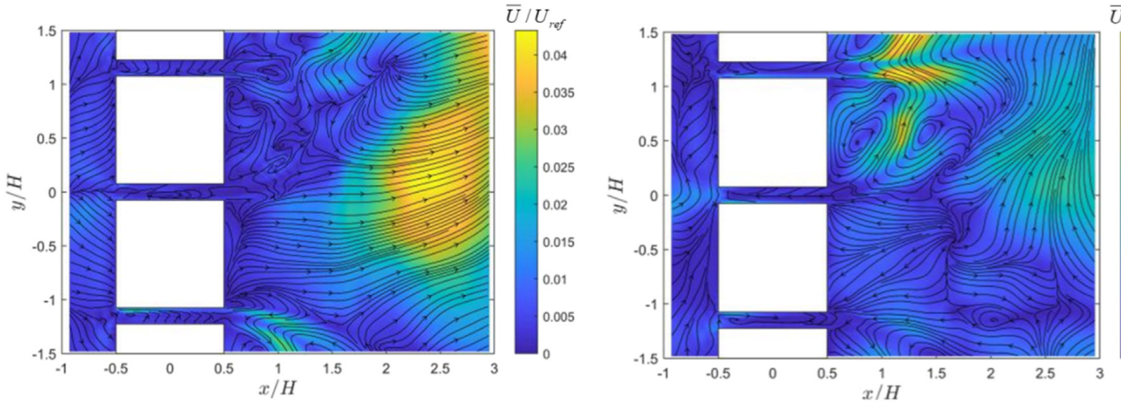

(a) DMD mode 1-2 (1.32 Hz) (b) DMD mode 3-4 (3.19 Hz)

FIG. 15. Normalized velocity vectors on the pedestrian-level plane at $z = 0.01$ m of (a) DMD mode 1–2 and (b) DMD mode 3–4 with respect to Type-b layout.

vortex scale in the Type-b layout is significantly smaller compared to the vortices observed in the other two layouts. Moreover, in contrast to Fig. 17(a), which exhibits a distinct wind corridor between two buildings, Figs. 17(c) and 17(e) do not display any discernible wind passage between the two structures. The layout of Type-b buildings may result in a rapid accumulation of pollutants in the surrounding area. Furthermore, the Type-1 mode under the Type-c layout also exhibits a pair of vortices behind the buildings, resembling the vortex pattern observed in the Type-a layout. However, the scale of the vortex is more akin to that of the Type-b layout. These vortex patterns share many similarities with the mean wind velocity field analysis in Sec. III A, which plays a crucial role in the accumulation of pollutants behind buildings.

3. Analysis of Type-2 POD–DMD–DFT mode for three building layouts

The vortex patterns of Type-2 mode exhibit a significant structural disparity when compared with the modes in Type-1. All of these modes correspond to a high mode frequency, which indicates that they are unstable in the timescale. The Type-2 mode, although serving as the primary energy contributor to the mean flow field, is limited in its influence on the evolution of large-scale vortices due to its unstable nature from a dynamic perspective. Moreover, these modes account for the transit acceleration phenomenon along the wind corridor in the middle of buildings, as depicted in Figs. 18(a) and 18(b). The wind corridor effect gradually diminishes as the relative distance between the middle of two buildings decreases, resulting in a decrease in pollutant removal efficiency when the space between the buildings is narrower. By adjusting the building layout to Type-c, the wind corridor emerges to the lateral sides of the building groups, enabling this unconventional configuration to sustain remarkably high levels of pollutant removal within a smaller coverage area.

The vortices in Type-2 POD–DMD–DFT mode exhibit reduced symmetry and increased chaotic behavior due to the shelter effect. The modes Type-2 generally consist of numerous small-scale vortices that exert their influence along the boundaries of the large-scale eddies

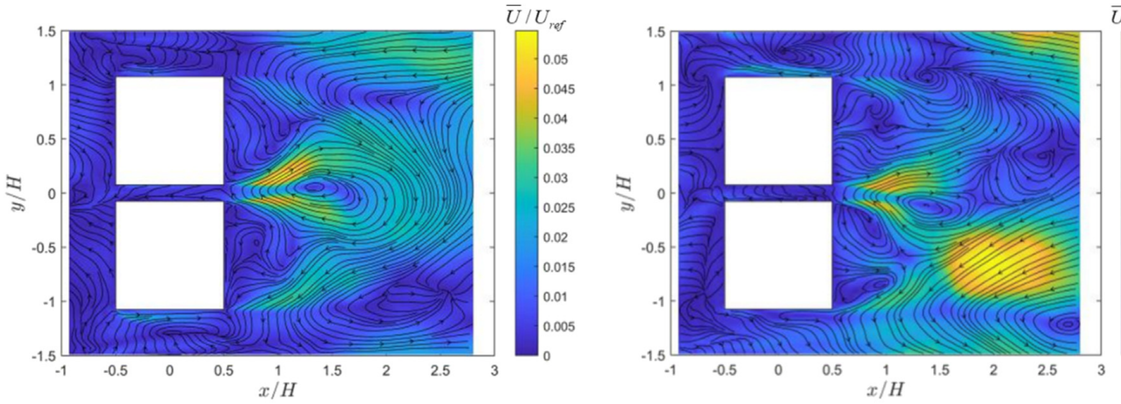

(a) DMD mode 1-2 (0.85 Hz) (b) DMD mode 3-4 (1.44 Hz)

FIG. 16. Normalized velocity vectors on the pedestrian-level plane at $z = 0.01$ m of (a) DMD mode 1–2 and (b) DMD mode 3–4 with respect to Type-c layout.

TABLE I. Frequency of classified modes and their corresponding mode type for different building layouts.

	Frequency	Mode type	Layout type
Mode 1–2	3.45	Type-1	Type-a
Mode 3–4	4.67	Type-1	Type-a
Mode 7–8	9.65	Type-3	Type-a
Mode 9–10	6.21	Type-2	Type-a
Mode 45–46	7.05	Type-2	Type-a
Mode 51–52	10.11	Type-2	Type-a
Mode 67–68	13.71	Type-2	Type-a
Mode 1–2	1.32	Type-1	Type-b
Mode 3–4	3.19	Type-1	Type-b
Mode 7–8	3.77	Type-3	Type-b
Mode 11–12	4.14	Type-3	Type-b
Mode 21–22	4.98	Type-2	Type-b
Mode 39–40	9.03	Type-2	Type-b
Mode 105–106	14.21	Type-2	Type-b
Mode 1–2	0.85	Type-1	Type-c
Mode 3–4	1.44	Type-1	Type-c
Mode 5–6	2.65	Type-1	Type-c
Mode 9–10	2.93	Type-3	Type-c
Mode 23–24	5.01	Type-2	Type-c
Mode 51–52	10.01	Type-2	Type-c
Mode 95–96	14.14	Type-2	Type-c

downstream of the buildings. The average scale of vortices in Type-2 is smaller compared to those in Type-1; however, a greater number of vortices are observed on the leeward side of the building. The continuous interaction and mutual dissipation among these small-scale vortices contribute to an expansion of the affected region behind buildings. The blockage effect at the upstream region of the buildings becomes more pronounced within the $0.2H$ region in the front of the buildings in Figs. 18(a) and 18(b), due to the acceleration effect instigated by resistance forces from the structure. Therefore, the presence of vortices in Type-b layout simultaneously reduced the turbulence intensity of upstream influence on the downstream region. The rapid formation and dissipation of these vortices in Type-2 mode have a limited impact on the gradual accumulation of pollutants behind the array of buildings.

4. Analysis of Type-3 POD–DMD–DFT mode for three building layouts

The Type-3 mode patterns with marginal energetic significance but remarkable dynamic influence with respect to different building layouts are summarized in Fig. 19. The dominant frequency of Type-3 modes is significantly lower compared to the frequency of Type-2 modes. A lower dominant frequency indicates a higher level of temporal stability and a more sustained vortex structure. Consequently, the energy contribution of Type-3 mode is comparatively lower than that of Type-1 mode, yet the influence of these modes on consistency persists for an extended duration. The vortex in Type-3 is primarily distributed from the wind corridor to the far end behind buildings, as a result of the interaction between the incoming flow and structures. The influence region of the vortices extends up to $3H$ behind the array of buildings, surpassing the reattachment point in the downstream region as depicted in Fig. 5, which provides strong evidence that Type-3 POD–DMD–DFT modes have limited contribution to the vortex pattern observed in the mean flow field.

The stability and downstream flow influence of the structures are generally determined by the width of the wind corridor. Vortex pairs reappear in Type-a and Type-c layouts, while vortices in Type-b layout exhibit reduced scale and increased chaotic behavior, resembling the outcome observed in Type-1 mode. The presence of these small-scale vortices hinders the movement of pollutant particles through the wind corridors between buildings, leading to the accumulation of pollutants in the downstream region of the structures. The Type-3 mode contributes to the formation of long-term reversed flow structures, which are observed behind the building clusters and in the wake region. These structures exhibit a slow velocity due to their relatively low energy contribution to the overall flow field; however, the vortex structure in Type-3 mode remains crucial in determining the turbulence field due to its gradual yet persistent accumulation of pollutants in the far-wake region.

It is important to acknowledge that the conclusion in Sec. III C cannot be solely deduced by analyzing the POD or DMD modes alone, as the POD modes are intricately intertwined with multiple dominant frequencies, and isolating DMD modes based on their contribution poses a challenge. Identifying the mode with the highest energy significance and continuous contribution remains unattainable. Therefore, through an analysis of the POD–DMD–DFT modes, a clear understanding can be obtained regarding how the spatial arrangement of buildings in an array influences pollutant accumulation in the wake region.

IV. CONCLUSION

The present study utilized LES to accurately simulate the flow field at the pedestrian level around various building layouts, while employing POD and DMD to extract the underlying coherent structure from the flow field data. Furthermore, modes imposing crucial effects on the flow field data from both energy and dynamical perspectives are successfully extracted using a model analysis method that combines POD and DMD techniques, namely POD–DMD–DFT augmented techniques. The main findings can be summarized as follows:

1. The arrangement of a building cluster significantly influences the turbulent flow pattern in its vicinity. A broader wind corridor can enhance the air ventilation performance at the rear of the building, thereby facilitating a reduction in the accumulation of pollutants downstream and an improvement in air quality.
2. The proposed POD–DMD–DFT methods address the limitations of both POD and DMD by extracting modes that play a crucial role in pollutant dispersion from both energetic and dynamic perspectives. This method compensates for the limitations of POD in capturing temporal variations in the flow field and addresses the energy contribution sequencing deficiency of DMD.
3. The Type-1 mode was found to govern the main velocity field and vortex patterns from the rear of the building to the reattachment point. The stable and continuous contribution from this mode sequentially transfers energy to the turbulence region. As

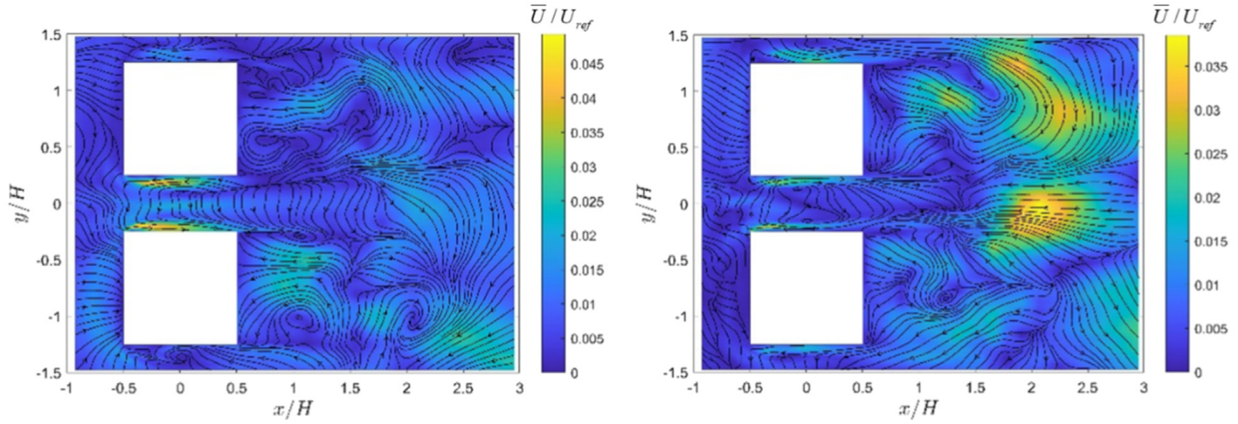

(a) Mode 1-2 (3.45 Hz) under Type-a layout (b) Mode 3-4 (4.67 Hz) under Type-a layout

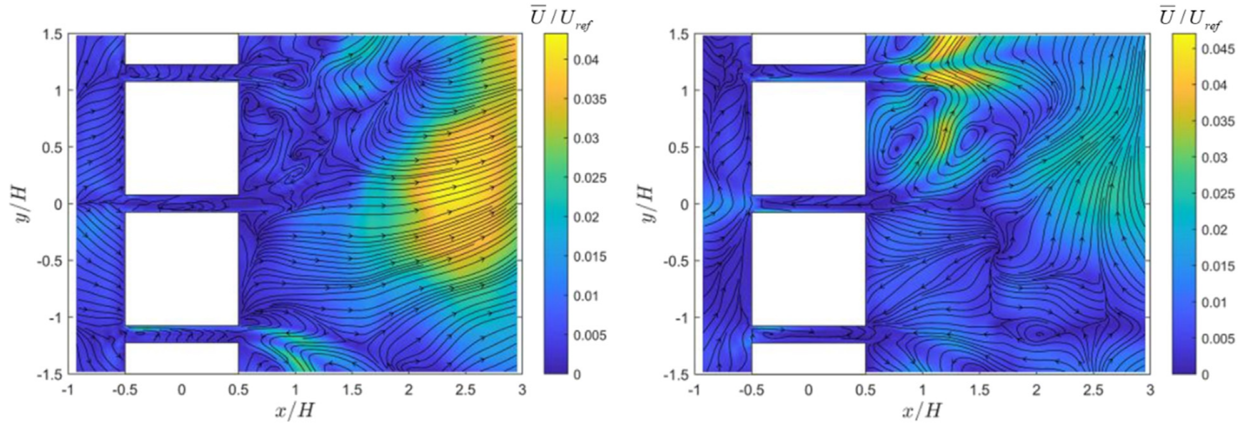

(c) Mode 1-2 (1.32 Hz) under Type-b layout (d) Mode 3-4 (3.19 Hz) under Type-b layout

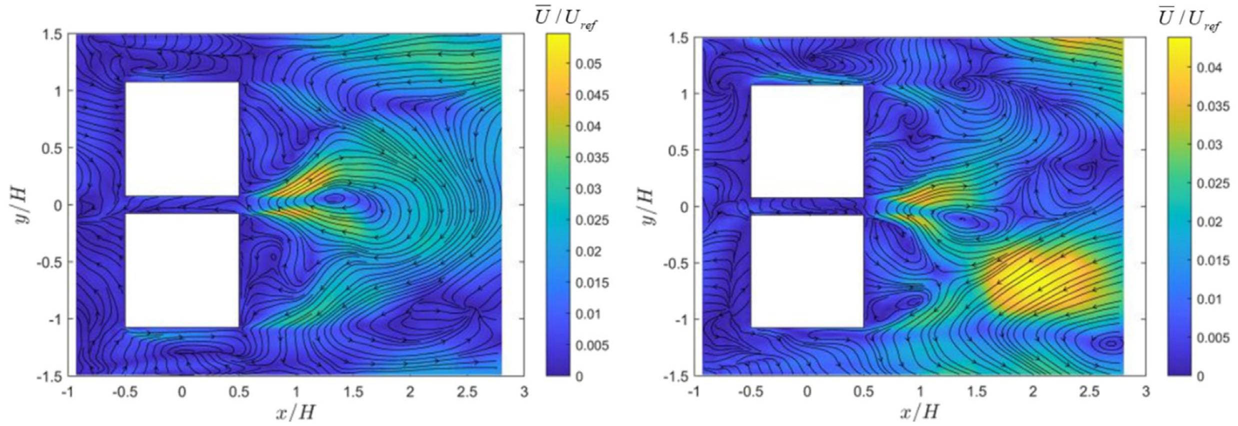

(e) Mode 1-2 (0.85 Hz) under Type-c layout (f) Mode 3-4 (1.44 Hz) under Type-c layout

FIG. 17. Normalized velocity vectors on the pedestrian-level plane at $z = 0.01$ m of Mode Type 1: (a) and (b) is Type-a layout; (c) and (d) is Type-b layout, and (e) and (f) is Type-c layout.

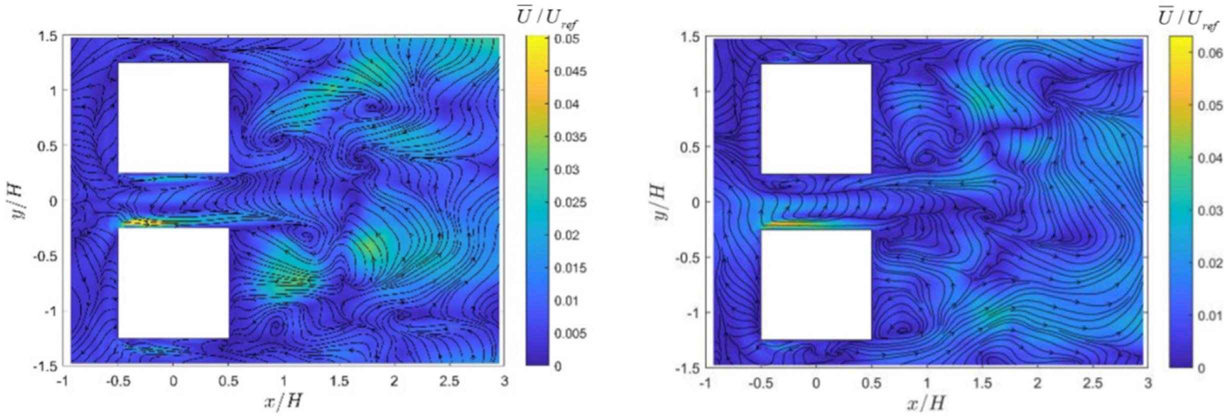

(a) Mode 9-10 (6.12 Hz) under Type-a layout (b) Mode 45-46 (7.05 Hz) under Type-a layout

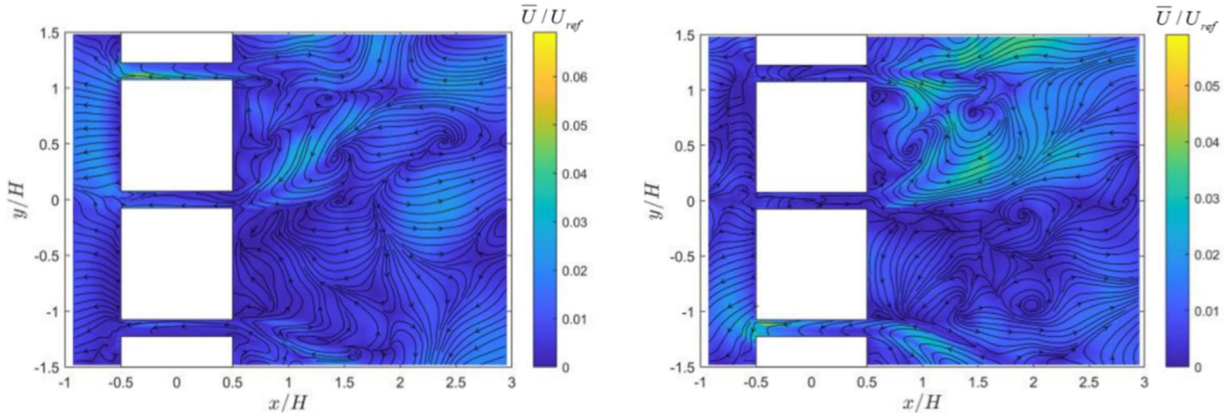

(c) Mode 21-22 (4.98 Hz) under Type-b layout (d) Mode 39-40 (9.03 Hz) under Type-b layout

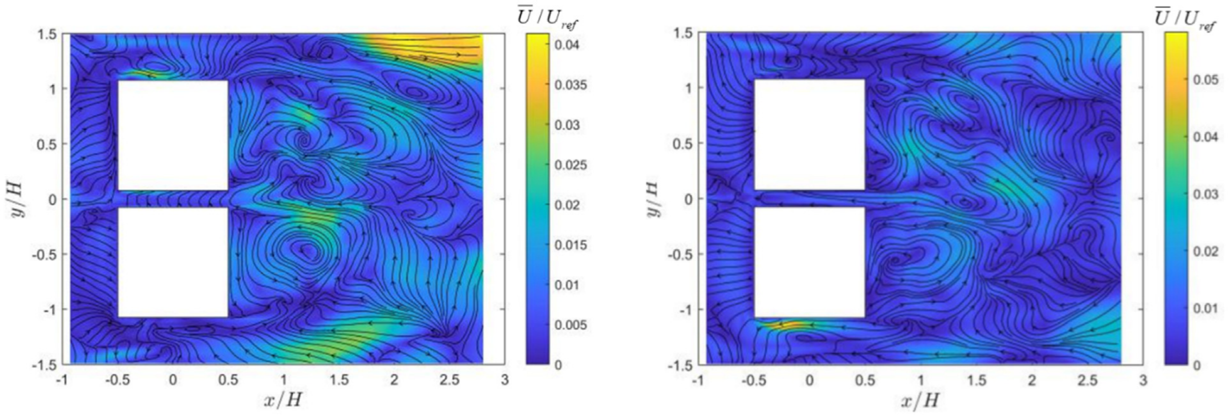

(e) Mode 23-24 (5.01 Hz) under Type-c layout (f) Mode 51-52 (10.01 Hz) under type-c layout

FIG. 18. Normalized velocity vectors on the pedestrian-level plane at $z = 0.01$ m of Mode Type 2: (a) and (b) is Type-a layout; (c) and (d) is Type-b layout, and (e) and (f) is Type-c layout.

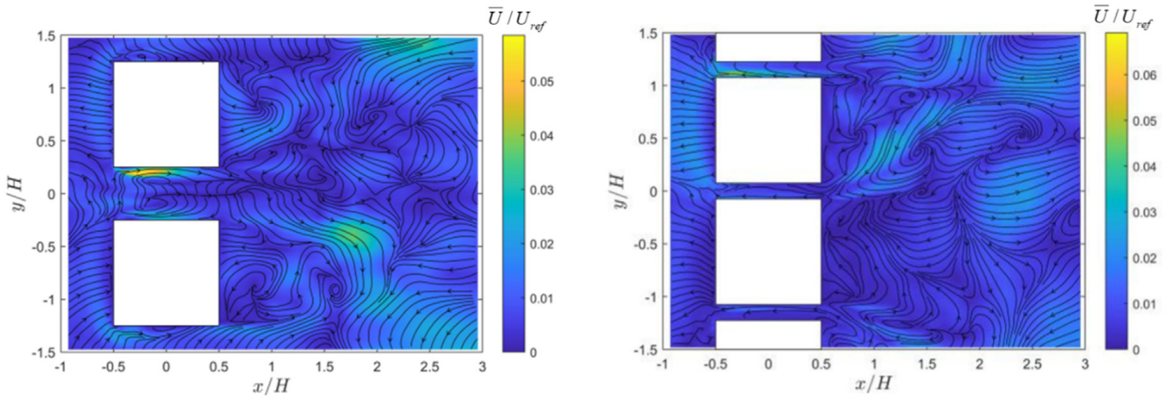

(a) Mode 7-8 (9.65 Hz) under Type-a layout (b) Mode 7-8 (3.77 Hz) under Type-b layout

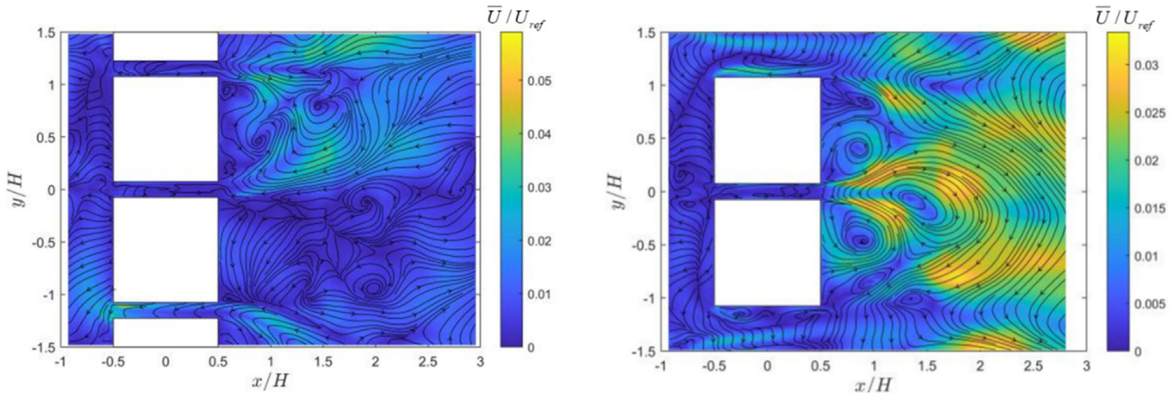

(c) Mode 11-12 (4.14 Hz) under Type-b layout (d) Mode 9-10 (2.93 Hz) under type-c layout

FIG. 19. Normalized velocity vectors on the pedestrian-level plane at $z = 0.01$ m of Mode Type 2: (a) is Type-a layout; (b) and (c) is Type-b layout, and (d) is Type-c layout.

buildings approach closer, the flow separation region in Type-1 mode becomes shorter, leading to a significant increase in wind velocity behind the reattachment point.

4. The Type-2 mode exhibits a higher prevalence of small-scale vortices compared to the Type-1 mode downstream of buildings. The influence exerted by these small vortices on the boundary of large-scale eddies gradually diminishes along the wind direction. The transit feature effectively mitigates the impact of Type-2 mode on the primary turbulence field. The identification of the highest TKE region through Type-2 mode enables periodic detection of sudden increases in pollutants near structures.
5. The Type-3 mode contributes a relatively low amount of energy to the overall flow field due to limited continuous energy transfer; however, it is crucial not to neglect these modes as their stable vortex structure can gradually and persistently impact the accumulation of pollutant concentration behind the building.

The present study addresses the research gap concerning the impacts of building layouts on pollutant dispersions by establishing the correlation between specific flow structures and the three dominant modes identified by the POD–DMD–DFT method. A more comprehensive understanding of the applications of POD–DMD–DFT methods in relation to wind fields, including pollutant dispersion and wind turbulence, can be achieved through future research utilizing the POD–DMD–DFT method. This innovative approach holds the potential for precise predictions and early warnings concerning urban pollutant dispersion fields.

Despite these contributions, this study was conducted with some limitations. This study primarily focuses on the velocity field and employs a qualitative analysis approach. However, it should be noted that the concentration field, which is highly relevant to pollutant dispersion, has not been considered in this research. The author will establish a future correlation between flow patterns and concentration variation modes by identifying consistent frequencies. For auxiliary analysis, the specific concentration variation patterns and velocity mode patterns will be taken into account. Future studies will also incorporate spectral proper orthogonal decomposition (SPOD) to investigate the concentration field surrounding building clusters.

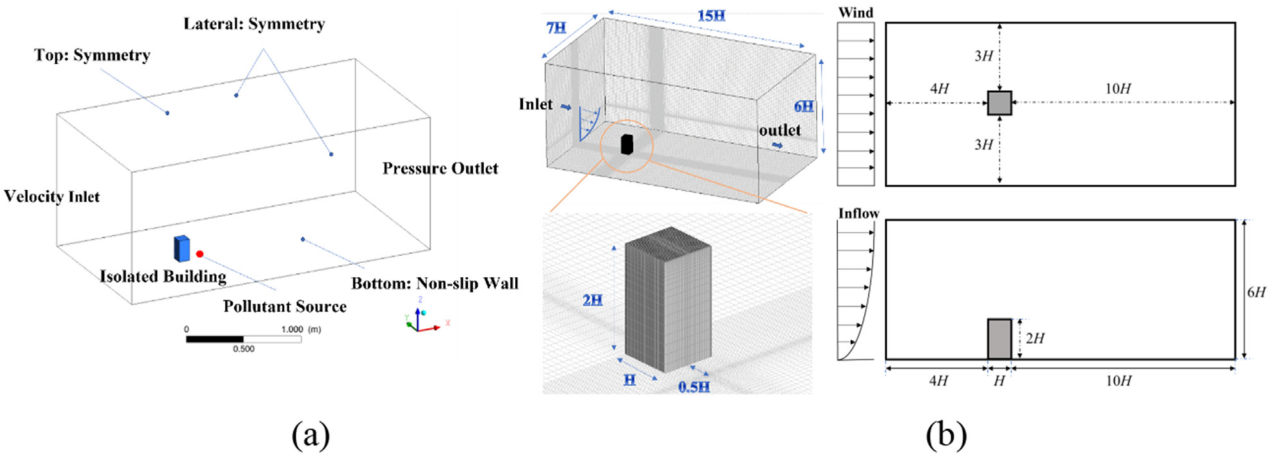

(a) (b)

FIG. 20. Schematics of (a) the boundary layer settings, and (b) dimensions of the building model and computational domain.

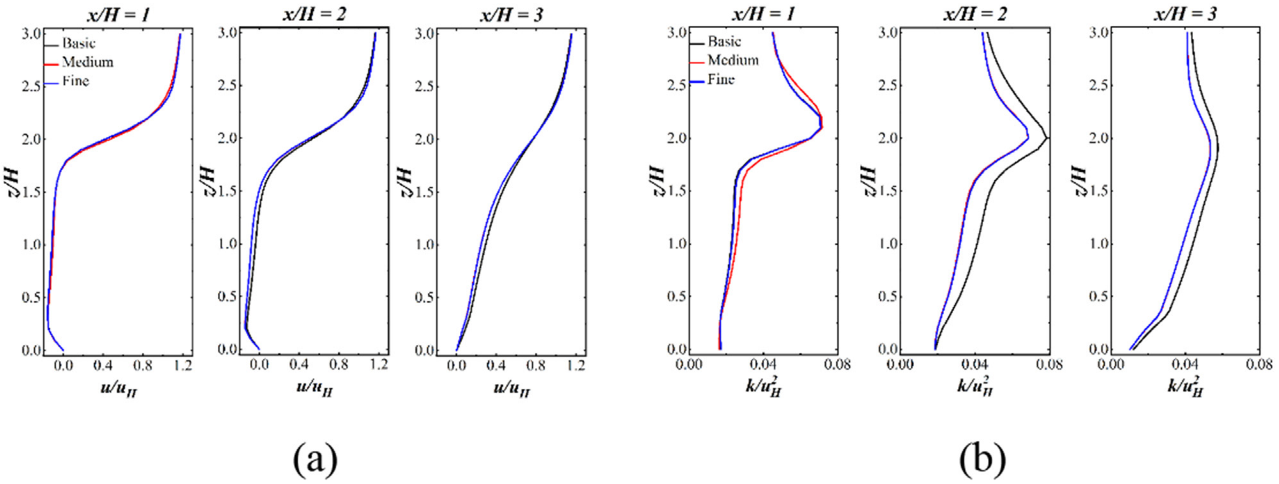

(a) (b)

FIG. 21. Comparison of (a) u/u_H and (b) k/u_H^2 values at lines $x/H = 1$, $x/H = 2$, and $x/H = 3$ for basic, medium, and fine grid arrangements.

ACKNOWLEDGMENTS

The work in this paper was supported by a grant from the Research Grants Council of Hong Kong Special Administrative Region, China (Project No. T22-504/21-R), the Fundamental Research Funds for the Central Universities of China [No. 0218005203003(17)], the Start-up Fund of Chongqing University [No. 02180011080006(3)], Supporting Scheme of Chongqing for Returned Overseas Chinese Entrepreneurial Start-ups [No. cx2023004(12)].

AUTHOR DECLARATIONS

Conflict of Interest

The authors have no conflicts to disclose.

Author Contributions

Cruz Y. Li contributed equally to this work.

Yunfei Fu: Formal analysis (equal); Methodology (equal); Project administration (equal); Writing – original draft (equal). **Cruz Y. Li:** Data curation (equal); Investigation (equal); Validation (equal); Writing – review & editing (equal). **Zhihang Zhao:** Formal analysis (equal); Writing – review & editing (equal). **Bingchao Zhang:** Conceptualization (equal); Methodology (equal); Resources (equal). **K. T. Tse:** Funding acquisition (equal); Supervision (equal). **Cheuk Ming Mak:** Conceptualization (equal); Methodology (equal). **Zengshun Chen:** Project administration (equal); Supervision (equal). **Xinxin Feng:** Formal analysis (equal); Writing – review & editing (equal). **Xisheng Lin:** Validation (equal); Writing – review & editing (equal). **Wenxin Li:** Visualization (equal); Writing – review & editing (equal). **Chongjia Lin:** Conceptualization (equal); Resources (equal); Supervision (equal); Validation (equal).

DATA AVAILABILITY

The data that support the findings of this study are available from the corresponding authors upon reasonable request.

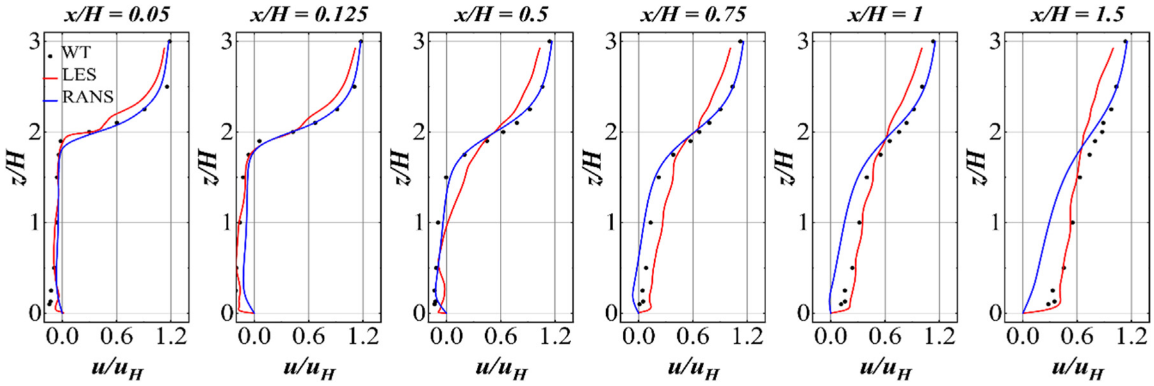

FIG. 22. Comparison of vertical profiles of dimensionless mean wind velocities with wind tunnel experiment results.

APPENDIX: ISOLATED BUILDING NUMERICAL VALIDATION

1. Building model description

To validate the accuracy of LES simulation, an isolated building model has been simulated and compared with the wind tunnel data conducted by Gorlé *et al.*[67] The building model has the dimensions of depth × width × height = $H \times H \times 2H$. The computational domain is with the dimension of $15H \times 7H \times 6H$, the domain inlet, ceiling, laterals, and outlet was 4 H, 4 H, 3 H, and 10 H away from the building models' boundary, respectively, as depicted in Fig. 20(b). Here, H is the depth of the building. The domain size and grid discretization obeyed the best practice guidelines of CFD simulations.[54] The point emission source was modeled at a distance of 0.5 H from the leeward side of the building's bottom.

2. Solver settings, grid sensitivity analysis and validation

The detailed ABL wind profile description refers to Sec. II D 2. First, RANS simulation was employed for all cases to obtain steady flow fields, providing initial conditions for LES. The PISO algorithm was employed in the LES simulations. Second-order discretization schemes were chosen to solve all convective and viscous terms in the governing equations. Moreover, the simulation was assumed to reach convergence for RANS when all residuals reach 10^{-6}, and that the residuals exhibit little variations with iteration.

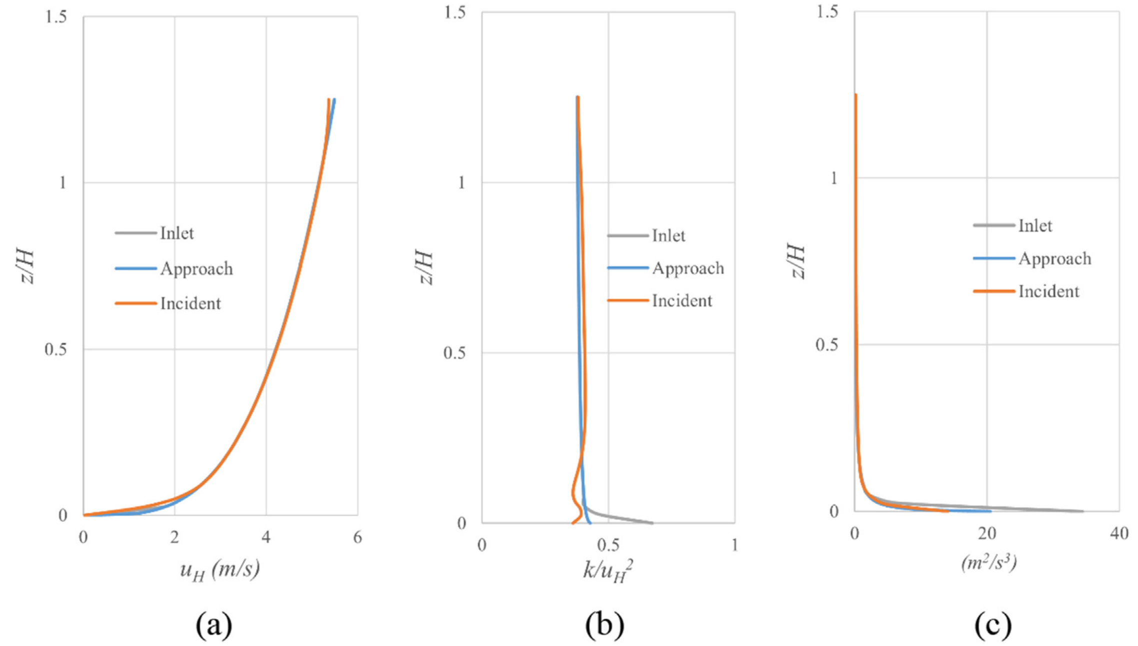

FIG. 23. Comparison of inlet, approach, and incident flow for (a) mean wind velocity, (b) TKE, and (c) turbulent dissipation rate.

Figure 21 compares the simulated u/u_H and k/u_H^2 at three horizontal lines ($x = H, 2H$, and $3H$) for basic, medium, and fine grid arrangement. u_H represents the reference wind velocity at the height of $z = H$. For normalized mean wind velocity, the results show that the medium grid configuration appears to be able to replicate the grid-independent flow field because the mean wind flow can be predicted with little deviation between the medium and fine grid arrangements. Furthermore, for the prediction of turbulence kinetic energy (TKE), although slight overestimation can be observed in the basic grid arrangement at $x/H = 2$ and 3, the medium and fine grid arrangement shows a high level of consistency and reproduces grid-independent flow field. Figure 22 compares the accuracy of the RANS and LES model results with the wind tunnel data.[56] The profiles indicate that LES results ideally predicted the velocity at $x/H = 0.05$, 0.125, 0.5, 0.75, 1, and 1.5.

3. Validation of the homogeneous ABL flow

Furthermore, the comparison is conducted between the inlet, approaching flow, and incident flow profile in order to analyze the homogeneity of the Atmospheric boundary layer (ABL) inflow, as illustrated in Fig. 23. The standard wall function[68] was utilized for the domain ground with a roughness height $C_s = 7$. The mean velocity profile and turbulent dissipation rate profile of the inlet flow exhibit a satisfactory concurrence with the approach flow and incident flow, thereby validating the credibility of the CFD inlet settings. Though a minimal discrepancy is observed in the TKE profile near the ground, the TKE at the pedestrian level of interest demonstrates a high level of consistency. Overall, the mean errors between the inlet flow and incident flow in terms of mean velocity, turbulent kinetic energy, and turbulent dissipation rate are 0.08, 0.51%, and 0.07%, respectively.

REFERENCES

[1] C. K. Chan and X. Yao, "Air pollution in mega cities in China," Atmos. Environ. **42**(1), 1–42 (2008).

[2] Z. Luo, Y. Li, and W. W. Nazaroff, "Intake fraction of nonreactive motor vehicle exhaust in Hong Kong," Atmos. Environ. **44**(15), 1913–1918 (2010).

[3] Y. Zhang, C. Ou, L. Chen, L. Wu, J. Liu, X. Wang, H. Lin, P. Gao, and J. Hang, "Numerical studies of passive and reactive pollutant dispersion in high-density urban models with various building densities and height variations," Build. Environ. **177**, 106916 (2020).

[4] A. Ferrari, A. Kubilay, D. Derome, and J. Carmeliet, "The use of permeable and reflective pavements as a potential strategy for urban heat island mitigation," Urban Clim. **31**, 100534 (2020).

[5] P. Ghobadi and N. Nasrollahi, "Assessment of pollutant dispersion in deep street canyons under different source positions: Numerical simulation," Urban Clim. **40**, 101027 (2021).

[6] P. Rajagopal, R. S. Priya, and R. Senthil, "A review of recent developments in the impact of environmental measures on urban heat island," Sustainable Cities Soc. **88**, 104279 (2023).

[7] W. Y. Ng and C. K. Chau, "A modeling investigation of the impact of street and building configurations on personal air pollutant exposure in isolated deep urban canyons," Sci. Total Environ. **468–469**, 429–448 (2014).

[8] M. Scungio, L. Stabile, V. Rizza, A. Pacitto, A. Russi, and G. Buonanno, "Lung cancer risk assessment due to traffic-generated particles exposure in urban street canyons: A numerical modelling approach," Sci. Total Environ. **631–632**, 1109–1116 (2018).

[9] J.-J. Baik and J.-J. Kim, "A numerical study of flow and pollutant dispersion characteristics in urban street canyons," J. Appl. Meteorol. Climatol. **38**(11), 1576–1589 (1999).

[10] S.-J. Park, J.-J. Kim, M. J. Kim, R. J. Park, and H.-B. Cheong, "Characteristics of flow and reactive pollutant dispersion in urban street canyons," Atmos. Environ. **108**, 20–31 (2015).

[11] Z. Shen, B. Wang, G. Cui, and Z. Zhang, "Flow pattern and pollutant dispersion over three dimensional building arrays," Atmos. Environ. **116**, 202–215 (2015).

[12] B. Blocken, "Computational fluid dynamics for urban physics: Importance, scales, possibilities, limitations and ten tips and tricks towards accurate and reliable simulations," Build. Environ. **91**, 219–245 (2015).

[13] L. Chen, C. M. Mak, J. Hang, Y. Dai, J. Niu, and K. T. Tse, "large eddy simulation study on pedestrian-level wind environments around elevated walkways and influential factors in ideal urban street canyons," Build. Environ. **235**, 110236 (2023).

[14] J. Liu, J. Niu, Y. Du, C. M. Mak, and Y. Zhang, "LES for pedestrian level wind around an idealized building array—Assessment of sensitivity to influencing parameters," Sustainable Cities Soc. **44**, 406–415 (2019).

[15] J. Liu, J. Niu, and Q. Xia, "Combining measured thermal parameters and simulated wind velocity to predict outdoor thermal comfort," Build. Environ. **105**, 185–197 (2016).

[16] Y. Toparlar, B. Blocken, B. Maiheu, and G. J. F. van Heijst, "A review on the CFD analysis of urban microclimate," Renewable Sustainable Energy Rev. **80**, 1613–1640 (2017).

[17] X. Li, C. Liu, D. Leung, and K. Lam, "Recent progress in CFD modelling of wind field and pollutant transport in street canyons," Atmos. Environ. **40**(29), 5640–5658 (2006).

[18] M. J. Davidson *et al.*, "Plume dispersion through large groups of obstacles—A field investigation," Atmos. Environ. **29**(22), 3245–3256 (1995).

[19] R. Macdonald, R. Griffiths, and D. Hall, "A comparison of results from scaled field and wind tunnel modelling of dispersion in arrays of obstacles," Atmos. Environ. **32**(22), 3845–3862 (1998).

[20] Y. Tominaga and T. Stathopoulos, "CFD simulation of near-field pollutant dispersion in the urban environment: A review of current modeling techniques," Atmos. Environ. **79**, 716–730 (2013).

[21] Q. Yang, T. Zhou, B. Yan, P. Van Phuc, and W. Hu, "LES study of turbulent flow fields over hilly terrains—Comparisons of inflow turbulence generation methods and SGS models," J. Wind Eng. Ind. Aerodyn. **204**, 104230 (2020).

[22] E. Yee, R. M. Gailis, A. Hill, T. Hilderman, and D. Kiel, "Comparison of wind-tunnel and water-channel simulations of plume dispersion through a large array of obstacles with a scaled field experiment," Boundary-Layer Meteorol. **121**(3), 389–432 (2006).

[23] M. Lateb, C. Masson, T. Stathopoulos, and C. Bédard, "Comparison of various types of k–ε models for pollutant emissions around a two-building configuration," J. Wind Eng. Ind. Aerodyn. **115**, 9–21 (2013).

[24] Y.-d. Huang, S.-q. Ren, N. Xu, Y. Luo, C. H. Sin, and P.-Y. Cui, "Impacts of specific street geometry on airflow and traffic pollutant dispersion inside a street canyon," Air Qual., Atmos. Health **15**(7), 1133–1152 (2021).

[25] P.-Y. Cui, R. Ji, L. He, Z. Zhang, Y. Luo, Y. Yang, and Y.-D. Huang, "Influence of GI configurations and wall thermal effects on flow structure and pollutant dispersion within urban street canyons," Build. Environ. **243**, 110646 (2023).

[26] Y. Guo, Q. Xiao, C. Ling, M. Teng, P. Wang, Z. Xiao, and C. Wu, "The right tree for the right street canyons: An approach of tree species selection for mitigating air pollution," Build. Environ. **245**, 110886 (2023).

[27] T. Shi, T. Ming, Y. Wu, C. Peng, Y. Fang, and R. de_Richter, "The effect of exhaust emissions from a group of moving vehicles on pollutant dispersion in the street canyons," Build. Environ. **181**, 107120 (2020).

[28] C. H. Sin, P.-Y. Cui, Y. Luo, K. S. Jon, and Y-d Huang, "CFD modeling on the canyon ventilation and pollutant exposure in asymmetric street canyons with continuity/discontinuity balconies," Atmos. Pollut. Res. **14**(1), 101641 (2023).

[29] L. Wang, J. Su, Z. Gu, and L. Tang, "Numerical study on flow field and pollutant dispersion in an ideal street canyon within a real tree model at different wind velocities," Comput. Math. Appl. **81**, 679–692 (2021).

[30] Y. Abbassi, H. Ahmadikia, and E. Baniasadi, "Prediction of pollution dispersion under urban heat island circulation for different atmospheric stratification," Build. Environ. **168**, 106374 (2020).

[31] J. Hang and Y. Li, "Ventilation strategy and air change rates in idealized high-rise compact urban areas," Build. Environ. **45**(12), 2754–2767 (2010).

[32] S. Hassan, U. H. Akter, P. Nag, M. M. Molla, A. Khan, and M. F. Hasan, "Large-eddy simulation of airflow and pollutant dispersion in a model street canyon intersection of Dhaka city," Atmosphere **13**(7), 1028 (2022).

[33] C. Miao, S. Yu, Y. Hu, R. Bu, L. Qi, X. He, and W. Chen, "How the morphology of urban street canyons affects suspended particulate matter concentration at the pedestrian level: An in-situ investigation," Sustainable Cities Soc. **55**, 102042 (2020).

[34] J. Ding and S.-J. Cao, "Identification of zonal pollutant diffusion characteristics using dynamic mode decomposition: Towards the deployment of sensors," Build. Environ. **206**, 108379 (2021).

[35] S. Ding and R. Yang, "Reduced-order modelling of urban wind environment and gaseous pollutants dispersion in an urban-scale street canyon," J. Saf. Sci. Resilience **2**(4), 238–245 (2021).

[36] S. Masoumi-Verki, F. Haghighat, and U. Eicker, "A review of advances towards efficient reduced-order models (ROM) for predicting urban airflow and pollutant dispersion," Build. Environ. **216**, 108966 (2022).

[37] J. Borggaard *et al.*, "Reduced-order modeling of turbulent flows," in Proceedings of MTNS, 2008.

[38] P. E. Bieringer, S. Longmore, G. Bieberbach, L. M. Rodriguez, J. Copeland, and J. Hannan, "A method for targeting air samplers for facility monitoring in an urban environment," Atmos. Environ. **80**, 1–12 (2013).

[39] F. Fang, T. Zhang, D. Pavlidis, C. C. Pain, A. G. Buchan, and I. M. Navon, "Reduced order modelling of an unstructured mesh air pollution model and application in 2D/3D urban street canyons," Atmos. Environ. **96**, 96–106 (2014).

[40] B. Sportisse and R. Djouad, "Use of proper orthogonal decomposition for the reduction of atmospheric chemical kinetics," J. Geophys. Res. **112**(D6), D06303, https://doi.org/10.1029/2006jd007808 (2007).

[41] E. Liberge and A. Hamdouni, "Reduced order modelling method via proper orthogonal decomposition (POD) for flow around an oscillating cylinder," J. Fluids Struct. **26**(2), 292–311 (2010).

[42] L. Zhou, K. T. Tse, G. Hu, and Y. Li, "Higher order dynamic mode decomposition of wind pressures on square buildings," J. Wind Eng. Ind. Aerodyn. **211**, 104545 (2021).

[43] F. Wang, K. M. Lam, G. B. Zu, and L. Cheng, "Coherent structures and wind force generation of square-section building model," J. Wind Eng. Ind. Aerodyn. **188**, 175–193 (2019).

[44] P. J. Schmid, "Dynamic mode decomposition of numerical and experimental data," J. Fluid Mech. **656**, 5–28 (2010).

[45] C. Y. Li, T. K. T. Tse, and G. Hu, "Dynamic mode decomposition on pressure flow field analysis: Flow field reconstruction, accuracy, and practical significance," J. Wind Eng. Ind. Aerodyn. **205**, 104278 (2020).

[46] H. Zhang, D. Xin, and J. Ou, "Wake control using spanwise-varying vortex generators on bridge decks: A computational study," J. Wind Eng. Ind. Aerodyn. **184**, 185–197 (2019).

[47] A. Guissart, T. Andrianne, G. Dimitriadis, and V. E. Terrapon, "Numerical and experimental study of the flow around a 4:1 rectangular cylinder at moderate Reynolds number," J. Wind Eng. Ind. Aerodyn. **189**, 289–303 (2019).

[48] J. N. Kutz, S. L. Brunton, B. W. Brunton, and J. Proctor, *Dynamic Mode Decomposition: Data-Driven Modeling of Complex Systems* (SIAM, 2016).

[49] J. Kou and W. Zhang, "An improved criterion to select dominant modes from dynamic mode decomposition," Eur. J. Mech.-B **62**, 109–129 (2017).

[50] K. Taira, S. L. Brunton, S. T. M. Dawson, C. W. Rowley, T. Colonius, B. J. McKeon, O. T. Schmidt *et al.*, "Modal analysis of fluid flows: An overview," AIAA J. **55**(12), 4013–4041 (2017).

[51] Y. Fu, X. Lin, L. Li, Q. Chu, H. Liu, X. Zheng, C.-H. Liu *et al.*, "A POD-DMD augmented procedure to isolating dominant flow field features in a street canyon," Phys. Fluids **35**(2), 025112 (2023).

[52] L. Sirovich, "Turbulence and the dynamics of coherent structures, Part I: Coherent structures," Q. Appl. Math. **45**(3), 561–571 (1987).

[53] K. M. Lam, M. Y. H. Leung, and J. G. Zhao, "Interference effects on wind loading of a row of closely spaced tall buildings," J. Wind Eng. Ind. Aerodyn. **96**(5), 562–583 (2008).

[54] Y. Tominaga, A. Mochida, R. Yoshie, H. Kataoka, T. Nozu, M. Yoshikawa, and T. Shirasawa, "AIJ guidelines for practical applications of CFD to pedestrian wind environment around buildings," J. Wind Eng. Ind. Aerodyn. **96**(10–11), 1749–1761 (2008).

[55] P. J. Richards and R. P. Hoxey, "Appropriate boundary conditions for computational wind engineering models using the k-ϵ turbulence model," J. Wind Eng. Ind. Aerodyn. **46–47**, 145–153 (1993).

[56] C. Gromke, R. Buccolieri, S. Di Sabatino, and B. Ruck, "Dispersion study in a street canyon with tree planting by means of wind tunnel and numerical investigations—Evaluation of CFD data with experimental data," Atmos. Environ. **42**(37), 8640–8650 (2008).

[57] D. K. Lilly, "The representation of small-scale turbulence in numerical simulation experiments," in Proceedings of the IBM Scientific Computing Symposium on Environmental Sciences, 1967.

[58] H. Wengle and H. Werner, "Large-eddy simulation of turbulence flow over and around a cube in a plate channel," in *Turbulent Shear Flows* (Springer, 1993), Vol. **8**, pp. 155–168.

[59] Y. Dai, C. M. Mak, Z. Ai, and J. Hang, "Evaluation of computational and physical parameters influencing CFD simulations of pollutant dispersion in building arrays," Build. Environ. **137**, 90–107 (2018).

[60] T. van Hooff, B. Blocken, and Y. Tominaga, "On the accuracy of CFD simulations of cross-ventilation flows for a generic isolated building: Comparison of RANS, LES and experiments," Build. Environ. **114**, 148–165 (2017).

[61] S. B. Pope, Turbulent Flows (Cambridge University Press, Cambridge, 2000).

[62] I. B. Celik, Z. N. Cehreli, and I. Yavuz, "Index of resolution quality for large eddy simulations," J. Fluids Eng. **127**(5), 949–958 (2005).

[63] B. Blocken, T. Stathopoulos, and J. Carmeliet, "Wind environmental conditions in passages between two long narrow perpendicular buildings," J. Aerosp. Eng. **21**(4), 280–287 (2008).

[64] O. Coceal, T. G. Thomas, I. P. Castro, and S. E. Belcher, "Mean flow and turbulence statistics over groups of urban-like cubical obstacles," Boundary-Layer Meteorol. **121**(3), 491–519 (2006).

[65] C. Y. Li, Z. Chen, T. K. T. Tse, A. U. Weerasuriya, X. Zhang, Y. Fu, and X. Lin, "A parametric and feasibility study for data sampling of the dynamic mode decomposition: Range, resolution, and universal convergence states," Nonlinear Dyn. **107**(4), 3683–3707 (2022).

[66] Q. Zhang, Y. Liu, and S. Wang, "The identification of coherent structures using proper orthogonal decomposition and dynamic mode decomposition," J. Fluids Struct. **49**, 53–72 (2014).

[67] C. Gorlé, J. van Beeck, P. Rambaud, and G. Van Tendeloo, "CFD modelling of small particle dispersion: The influence of the turbulence kinetic energy in the atmospheric boundary layer," Atmos. Environ. **43**(3), 673–681 (2009).

[68] B. E. Launder and D. B. Spalding, "The numerical computation of turbulent flows," Comput. Methods Appl. Mech. Eng. **3**(2), 269 (1974).